

## Propulsion Performance Comparison of Hardand Soft-Magnetic Microrobots Under Rotating Magnetic Fields

## Master's Thesis

Author: Joost Wijnmaalen

Supervisors: Iulian Apachitei, Leon Abelmann

Master's Program: Biomedical Engineering – Medical Devices

Dated: 11 July 2025



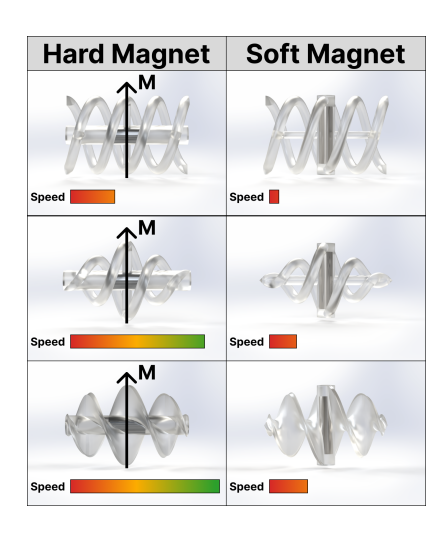
## **CONTENTS**

I.	Main Manuscript	1
n.	Supplementary Material 1: Magnetic Torque Calculations	8
m.	Supplementary Material 2: Magnetic Array Optimization	. 19
IV.	Supplementary Material 3: Microrobot Fabrication	. 43

# Propulsion Performance Comparison of Hard- and Soft-Magnetic Microrobots Under Rotating Magnetic Fields

Joost Wijnmaalen<sup>1</sup>, Leon Abelmann<sup>1</sup>, and Iulian Apachitei<sup>1</sup> Delft University of Technology, Delft, The Netherlands.

(Dated: 11 July 2025)



This study compares the propulsion performance between hard- and soft-magnetic microrobots under rotating magnetic fields. Results show that hard-magnetic microrobots achieved step-out frequencies and maximum propulsion speeds 4.5 times higher than softmagnetic microrobots. Below saturation magnetization, soft-magnetic microrobots demonstrated similar performance irrespective of magnetic susceptibility, highlighting that torque generation in these materials is purely geometry-dependent. Employing a tapered ribbon design increased propulsion speed by a factor of 3.5 compared to regular helical designs. These results provide a quantitative basis for selecting materials and designs, enabling designers to weigh the propulsion benefits of hard magnets against the biocompatibility of soft-magnetic microrobots.

#### **CONTENTS**

I.	Introduction	1
II.	Theory	2
	A. Magnetic Torque	2
	B. Microrobot Hydrodynamics	2
III.	Experimental	2
	A. Rotating Magnetic Field Generation	2
	B. Microrobot Design and Fabrication	3
	C. Microrobot Propulsion Evaluation	3
IV.	Results and Discussion	4
	A. Magnetic Material Comparison	4
	B. Microrobot Design Comparison	4
	D. Microrobot Design Comparison	4
$\mathbf{V}.$	Conclusions	5
	Acknowledgments	5
	References	6
Α.	Magnetic Field Validation	7

## I. INTRODUCTION

Over the past decade, microrobots have emerged as a versatile platform for biomedical applications, including the physical removal of blood clots and biofilms<sup>1,2</sup>, targeted drug delivery<sup>3</sup>, and thermal ablation of bacterial infections<sup>4</sup>.

Microrobots typically have a polymeric structure created through two-photon polymerization or microstereolithography<sup>5</sup>, and incorporate a magnetic component for torque-driven actuation. This enables precise microrobot control using tri-axial Helmholtz coil systems, and also allows for magnetic heating  $^{6,7}$ . The magnetic component can be made from either hardor soft-magnetic materials. Hard-magnetic materials are favored for their ability to generate high magnetic torques, with NdFeB as a typical choice<sup>8,9</sup>. However, NdFeB exhibits cytotoxic properties, necessitating careful consideration for in vivo use and subsequent removal<sup>10</sup>. In contrast, soft magnetic materials such as superparamagnetic iron oxide nanoparticles (SPIONs) are biocompatible but provide limited torque output, which might constrain their use<sup>3,11</sup>.

Despite these trade-offs, an experimental comparison between hard- and soft-magnetic microrobots has, to our knowledge, not been conducted. Such an analysis would contextualize the usability of magnetic materials already used in microrobots, such as NdFeB and SPIONs, and validate the integration of novel materials such as biodegradable pure Fe, which could be incorporated as thin wires down to  $25 \, \mu m$ . Therefore, this study addresses the research question:

"How do hard- and soft-magnetic microrobots compare in propulsion performance under rotating magnetic fields?"

To enable comparison, three distinct microrobot geometries were each fabricated with three different magnetic materials: NdFeB (hard-magnetic), ferrite (soft-magnetic), and pure Fe (soft-magnetic). This

resulted in nine unique microrobots, all 10 mm in length. Each was actuated in a 20 mT rotating magnetic field. Propulsion tests were conducted in glycerin, chosen for its high viscosity to achieve low Reynolds number conditions similar to those expected for smaller microrobots in future applications<sup>12</sup>.

#### II. THEORY

#### A. Magnetic Torque

For hard-magnetic microrobots, magnetic torque arises from the tendency of the magnet's fixed magnetization to align with an external magnetic field. Maximum torque is reached when the magnetization and field are perpendicular, and is given by<sup>13</sup>:

$$T_{\text{max}}^{\text{hard}} = \mu_0 V M H_0 \text{ (N m)}, \qquad (1)$$

where  $\mu_0$  is the vacuum permeability  $(N/A^2)$ , V the volume of the magnetic element  $(m^3)$ , M the magnetization (A/m), and  $H_0$  the external magnetic field strength (A/m).

In soft-magnetic microrobots, torque arises from shape anisotropy. Shape anisotropy depends on geometry, favoring alignment of the material's long axis with the external magnetic field to minimize magnetic energy. When an external magnetic field is applied at an angle to this axis, torque is generated. Embedding a soft-magnetic cylinder perpendicular to the microrobot's movement direction induces propulsive torque. Maximum torque is reached when the external magnetic field is angled 45° relative to the long axis of the soft-magnetic material, and is defined by 14:

$$T_{\text{max}}^{\text{soft}} = \frac{\mu_0 V H_0^2 (n_{\text{r}} - n_{\text{a}})}{2n_{\text{a}} n_{\text{r}}} (\text{N m}) .$$
 (2)

Here,  $n_r$  and  $n_a$  represent the demagnetization factors in the radial and axial (long) directions, respectively, which can be approximated with ellipsoid demagnetization factors. This equation is valid only when the internal magnetization remains below saturation, defined as:

$$H_{\text{low}} = \frac{M_{\text{s}} n_a n_r \sqrt{2}}{\sqrt{n_a^2 + n_r^2}} \,(\text{A/m}) \,,$$
 (3)

where  $M_s$  is the saturation magnetization (A/m). For  $H_0 > H_{low}$ , other torque equations apply, which are provided in Supplementary Material 1 together with the derivations of Equations 1–3.

## B. Microrobot Hydrodynamics

The maximum speed of helical microrobots, propelled by magnetic torque in viscous environments

(Re  $\ll 1$ ), is given by<sup>15</sup>:

$$v_{\text{max}} = -\frac{b}{a}\omega_{\text{max}} \text{ (m/s)} . \tag{4}$$

Here, a represents the resistance to forward motion (Ns/m), and b denotes the coupling between rotation and translation (Ns), both dependent on microrobot geometry and fluid viscosity.  $\omega_{\rm max}$  (Hz) is the highest rotational frequency at which the microrobot can maintain synchronous rotation with the external magnetic field. The rotational frequency at which synchrony is lost is called the step-out frequency  $\omega_{\rm so}$ , and is given by:

$$\omega_{\rm so} = \frac{a}{ac - b^2} T_{\rm max} \, (Hz) \,, \tag{5}$$

where c is the rotational resistance (N s m) and  $T_{\text{max}}$  is the maximum available magnetic torque (N m).

To analyze how the maximum speed of a microrobot scales with size and viscosity, geometric similarity is assumed using a scaling factor  $\lambda$ . Coefficients a, b, and c scale as  $\lambda\eta$ ,  $\lambda^2\eta$ , and  $\lambda^3\eta$ , respectively. Furthermore, magnetic torque, whether originating from hard (Equation 1) or soft magnets (Equation 2), scales as  $\lambda^3$  due to its dependence on volume. Inserting these scaling relationships into Equations 4 and 5 results in:

$$v_{\rm max} \propto \frac{\lambda}{\eta} \ .$$
 (6)

This demonstrates that the maximum speed scales linearly with helix size and inversely with viscosity. For example, scaling a 10 mm robot to 100  $\mu$ m and reducing the fluid viscosity from 1 Pas to 5 mPas would increase  $v_{\rm max}$  by a factor of 2, assuming all other parameters remain unchanged.

## III. EXPERIMENTAL

## A. Rotating Magnetic Field Generation

The goal of the setup shown in Figure 1, was to generate a uniform rotating magnetic field of  $20\,\mathrm{mT}$  over a  $120\,\mathrm{mm}$  region to enable microrobot propulsion. This system serves as a cost-effective alternative to traditional Helmholtz coil setups. The magnetic field was generated using two identical arrays ( $175\times30\,\mathrm{mm}$ ), each consisting of 3 rows and 18 columns of  $5\times5\times5\,\mathrm{mm}$  N42 NdFeB magnets (supermagnete, Gottmadingen, Germany). The distance between the opposing magnets was optimized using the Adam algorithm from the Optax library in Python<sup>16</sup>. The resulting array was 3D printed using a Bambu Lab X1C, and the individual magnets were secured via press fit. A uniform field strength of  $20\,\mathrm{mT}$  was confirmed (Appendix A) using a Lake Shore  $455\,\mathrm{DSP}$ 

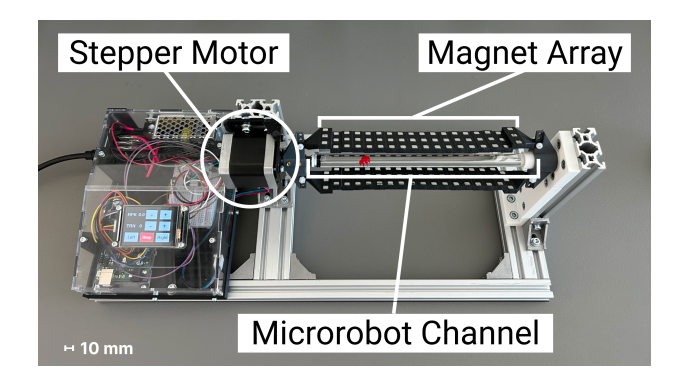


FIG. 1. Rotating magnetic field setup for generating uniform magnetic torque to propel microrobots.

Gaussmeter. Additional details about the optimization and construction of the magnetic arrays are included in Supplementary Material 2. The magnetic arrays were mounted on a hollow axle which held a channel containing glycerin, with a viscosity of 1.14 Pas. The magnetic arrays were rotated using a stepper motor and controlled through a touchscreen connected to an Arduino Uno. To ensure safe operation, the stepper motor was restricted to a maximum rotational frequency of 5 Hz.

#### B. Microrobot Design and Fabrication

One hard-magnetic microrobot, NdFeB (N42; first4magnets, Sutton-in-Ashfield, United Kingdom), and two soft-magnetic microrobots, ferrite (78 material; Fair-Rite, Wallkill, United States) and pure Fe (99.5% purity; Goodfellow, Huntingdon, United Kingdom), were tested (Figure 2). Two soft-magnetic microrobots were tested to assess the influence of magnetic susceptibility on torque generation. The NdFeB magnet measured 3 mm in length and 1 mm in diameter and had a remanent magnetization of 1.30 T. The ferrite and pure Fe samples were 5.33 mm long and 0.75 mm in diameter to match the magnetic volume of the NdFeB magnet, with magnetic susceptibilities of 3000 and 8000, respectively. The saturation magnetization of 99.5% pure Fe is 1.8T and 0.48 T for 78 material ferrite. Three microrobot designs from literature were tested: a double helix, a tapered double helix, and a tapered ribbon-shaped design<sup>17</sup>. All designs were 10 mm in length. The double helix had a constant width of 6.5 mm and a coil diameter of 0.8 mm. The tapered helix had the same length and maximum width but featured a 30° taper from both ends toward the center. The ribbon-shaped design consisted of a 0.3 mm thick twisted plate with a central width of 6.5 mm, tapered from both ends toward the center, also at a 30° angle.

The microrobots were designed in SolidWorks, processed using PreForm slicing software, and printed

	NdFeB Hard Magnet	Ferrite Soft Magnet	Pure Fe Soft Magnet
Helix	M H 1 mm	H 1mm	H 1mm
Tapered Helix	M H 1 mm	H 1 mm	H1mm
Tapered Ribbon	M H 1 mm	H1mm	H1mm

FIG. 2. Tested hard- and soft-magnetic microrobot designs, each 10 mm long, with matched magnetic volumes.

on a Formlabs Form 3 stereolithography printer with clear V4 resin. Printed structures were washed in isopropanol (Form Wash, Formlabs; 10 min), post-cured (Form Cure, Formlabs; 30 min), and support marks were manually removed using 800-grit sandpaper. Magnetic materials were secured using UHU Magnet Glue (UHU GmbH & Co. KG, Bühl, Germany). For full fabrication details, see Supplementary Material 3.

The 3D models of all microrobot designs, corresponding PreForm files, the 3D model of the test setup, wiring diagrams, bill of materials, and optimization code are available on GitHub.

### C. Microrobot Propulsion Evaluation

Propulsion characteristics were determined by recording the microrobot's motion over a 100 mm path at 0.1 Hz intervals using an iPhone 14 camera at 60 fps (see Supplementary Material 4). The camera was placed at the center of the magnetic arrays at a distance of 120 mm. The entry and exit frames were used to determine the travel time and compute the speed. A linear fit was applied to the speed measurements up to the rotation frequency at which half the maximum speed was reached. Subsequently, the 95% confidence interval of the measurements was determined by:

$$\Delta v_i = 1.96 v_i \sqrt{\left(\frac{\text{RMSE}}{\bar{v}}\right)^2 + \left(\frac{\sigma_d}{L}\right)^2} \quad (\text{m/s}) , \qquad (7)$$

where  $\Delta v_i$  is the half-width of the 95% confidence interval for the *i*-th speed measurement,  $v_i$  is the corresponding speed, RMSE is the root-mean-square error of the linear fit applied to the first 50% of data points up to maximum speed,  $\bar{v}$  is the mean speed over that range,  $\sigma_d$  is the distance measurement uncertainty, and L is the nominal measurement length. The stepout frequency was defined as the lowest rotational

TABLE I. Comparison of step-out frequency  $\omega_{\rm so}$  and maximum speed  $v_{\rm max}$  with embedded hard- or soft-magnetic elements in three different microrobot designs.

Design	Magnet Type	Material	$\omega_{ m so} \ {f Hz}$	$v_{ m max} \over  m mm/s$
Helix	Hard Soft Soft	NdFeB Ferrite Pure Fe	4.4(2) 1.2(1) 1.1(1)	$ 2.7(2) \\ 0.6(1) \\ 0.6(1) $
Tapered Helix	Hard	NdFeB	> 5.0	> 2.8
	Soft	Ferrite	3.2(1)	1.7(1)
	Soft	Pure Fe	3.1(1)	1.7(1)
Tapered Ribbon	Hard	NdFeB	> 5.0	> 6.2
	Soft	Ferrite	2.4(1)	2.1(1)
	Soft	Pure Fe	2.3(1)	2.0(1)

frequency at which three consecutive speed measurements, including their confidence intervals, fell entirely below the linear fit.

### **RESULTS AND DISCUSSION**

#### Magnetic Material Comparison

Table I summarizes the step-out frequencies and maximum propulsion speeds for all tested materials and designs. Notably, hard-magnetic (NdFeB) microrobots achieved higher step-out frequencies and corresponding maximum speeds compared to softmagnetic (ferrite and pure Fe) variants. Table I also shows that both soft-magnetic materials exhibited similar propulsion performance despite having different magnetic susceptibilities. This aligns with the findings of Abbott et al. 14, who reported that torque generation in soft-magnetic materials is insensitive to magnetic susceptibility. This holds true as long as the magnetic material remains unsaturated. Since commercially available Helmholtz coil systems typically operate below 20 mT, magnetic saturation is unlikely to occur when using such systems for microrobot propulsion.

## Microrobot Design Comparison

Figure 3 shows that hard-magnetic helical microrobots achieved a maximum speed 4.5 times higher than both soft-magnetic designs, which aligns with torque predictions based on Equations 1 and 2 (see Supplementary Material 1). The observed 4.5-fold difference in step-out frequency and maximum speed is expected to persist when scaling to a size more relevant for biomedical applications due to similar low Reynolds numbers. Specifically, when scaling from the current 10 mm microrobot in glycerin

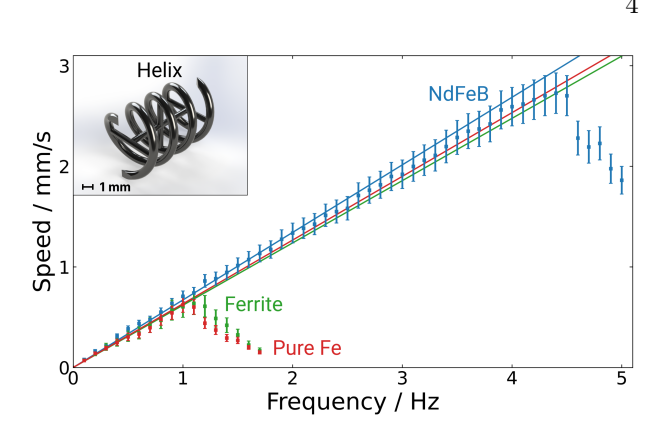


FIG. 3. Measured translation speed as a function of external magnetic field rotation frequency for one hardmagnetic (NdFeB) and two soft-magnetic (ferrite and pure Fe) helical microrobots. All designs exhibited similar linear behavior up to their step-out frequency, with the hard-magnetic helix achieving a step-out frequency and maximum speed 4.5 times higher compared to the soft-magnetic designs.

 $(\eta = 1.14 \,\mathrm{Pa\,s})$  to a  $100 \,\mathrm{\mu m}$  microrobot in blood  $(\eta = 5 \,\mathrm{mPa\,s})$ , the Reynolds number remains low (Re  $\ll 1$ ). The nearly identical propulsion efficiencies (slope: 0.65) of the hard- and soft-magnetic helical designs also indicate that the orientation of the magnetic material, whether along the length or width of the microrobot, has minimal effect on propulsion characteristics. Interestingly, the relationship between rotational frequency of the magnetic field and translational speed became nonlinear approaching maximum speed. This behavior contrasts with the fully linear response reported by Wang et al. 15. The observed gradual loss of linearity likely results from subtle local variations in the magnetic field or from local increases in drag due to occasional wall contact. Both effects can cause the microrobot to reach the step-out frequency earlier in specific regions along its propulsion path. However, these deviations remained small, indicating minimal wall contact and underscoring the overall uniformity of the generated magnetic field.

The tapered helix achieved the highest step-out frequency among all soft-magnetic designs, but also had the lowest propulsion efficiency (slope: 0.57), as can be seen in Figure 4. This enhancement in speed and step-out frequency is attributed to the reduced width and increased spacing between the microrobot and surrounding surfaces, which decreases rotational friction. Although this design slightly compromises propulsion efficiency, the threefold increase in maximum speed outweighs this reduction. It should be noted that the step-out frequency of hard-magnetic tapered helices exceeded the experimental limit of 5 Hz, preventing direct confirmation of the three-fold increase in step-out frequency and maximum speed. Lowering the magnetic field strength could bring the

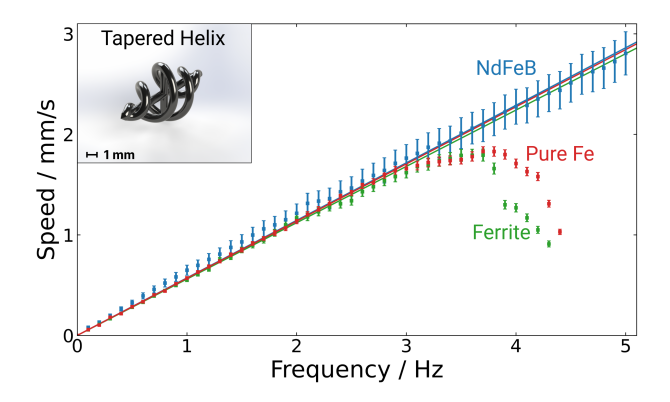


FIG. 4. Measured translation speed as a function of external magnetic field rotation frequency for one hard-magnetic (NdFeB) and two soft-magnetic (ferrite and pure Fe) tapered helical microrobots. This design achieved a threefold increase in step-out frequency and maximum speed compared to regular helical designs.

step-out frequency within the experimental limit of 5 Hz. However, this would reduce the number of data points available for the linear fit, compromising the accuracy of the results, and was therefore not pursued. Given the identical slopes and torque-dependent propulsion behavior observed in the regular helical designs, however, it is likely that a similar threefold increase applies to the hard-magnetic tapered helical designs. Furthermore, the higher rotational speeds of this design may also improve the physical ablation of structures with shear-thinning properties, such as biofilms<sup>18</sup>. However, further research is needed to quantify this effect.

Figure 5 shows that the tapered ribbon achieved the highest maximum speed among all tested designs, which could shorten procedure times in biomedical applications. Its step-out frequency was twice that of the regular helix, while its maximum speed was 3.5 times greater. Despite having a step-out frequency lower than the tapered helix, the tapered ribbon achieved the highest maximum speed. This underscores the intricate relationship between rotational resistance and propulsion. The larger surface area of the ribbon-shaped design may also allow for greater drug loading and faster release. Interestingly, a small but statistically significant efficiency gap was observed between hard- and soft-magnetic ribbon-shaped designs. This likely occurred because the thinner ribbon walls made the transverse rods in the soft-magnetic designs contribute more to drag. In contrast, the thicker overall structure of the helical designs resulted in minimal additional drag from the transverse rod. Nevertheless, the ribbon-shaped designs achieved the highest maximum speed of all tested microrobots.

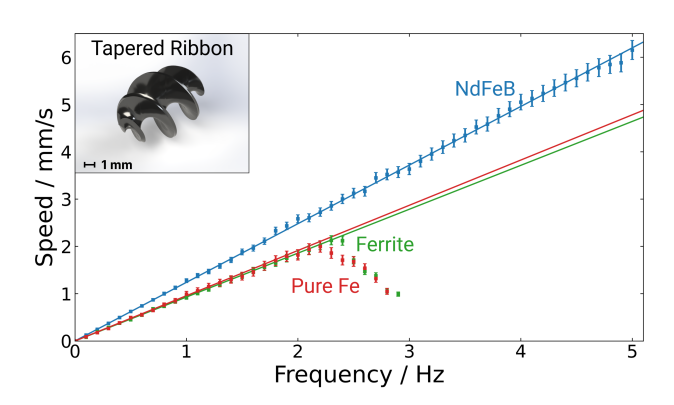


FIG. 5. Measured translation speed as a function of external magnetic field rotation frequency for one hard-magnetic (NdFeB) and two soft-magnetic (ferrite and pure Fe) ribbon-shaped microrobots. This design achieved the highest maximum speeds among all designs.

### V. CONCLUSIONS

Helical microrobots incorporating hard-magnetic materials outperform soft-magnetic microrobots under rotating magnetic fields, achieving a 4.5-fold higher step-out frequency and corresponding maximum propulsion speed under matched magnetic volume, field strength, and viscosity at low Reynolds numbers. Notably, for soft-magnetic materials, the generated torque is independent of magnetic susceptibility, resulting in identical propulsion characteristics for comparable geometric designs below the saturation field. Furthermore, employing a tapered ribbon-shaped design was shown to improve maximum propulsion speed by a factor of 3.5 compared to a regular helical design, underscoring the influence of geometry on microrobot performance.

These performance differences provide a quantitative basis for informed material and design selection. This enables designers to balance the propulsion advantages of hard magnets against the biocompatibility of soft-magnetic alternatives. It also allows them to select the most suitable geometric design for their application. Future work should explore microrobot functionalities beyond propulsion, with a particular focus on heating efficiency for thermal ablation and controlled drug release. Comparing hard- and soft-magnetic materials in this context would offer a more comprehensive understanding of their respective advantages and limitations, ultimately guiding the design and application of microrobots for specific clinical tasks.

## **ACKNOWLEDGMENTS**

The authors thank Sander Leeflang and Jinlai Li for their assistance with 3D printing the microrobots.

### **REFERENCES**

- <sup>1</sup>M. C. J. de Boer, L.-J. W. Ligtenberg, I. Mulder, and C. Goulas, Applied Physics Reviews 12, 011416 (2025).
- <sup>2</sup>H. H. Tran, A. Watkins, M. J. Oh, A. Babeer, T. P. Schaer, E. Steager, and H. Koo, Trends in Biotechnology 10.1016/j.tibtech.2023.10.004 (2023).
- <sup>3</sup>H. Ceylan, I. C. Yasa, O. Yasa, A. F. Tabak, J. Giltinan, and M. Sitti, ACS Nano 13, 3353 (2019).
- <sup>4</sup>C. Chen, L. Chen, Y. Yi, C. Chen, L.-F. Wu, and T. Song, Applied and Environmental Microbiology **82**, 2219 (2016).
- <sup>5</sup> J. Li and M. Pumera, Chemical Society Reviews 50, 2794 (2021).
- <sup>6</sup>B. Nelson, J. Abbott, K. Peyer, M. Cosentino, L. Zhang, L. Dong, and I. Kaliakatsos, The International Journal of Robotics Research 28, 1434 (2009).
- <sup>7</sup>M. Sitti and D. S. Wiersma, Advanced Materials (Deerfield Beach, Fla.) **32**, e1906766 (2020).
- <sup>8</sup>Z. Ren, W. Hu, X. Dong, and M. Sitti, Nature Communications **10**, 2703 (2019).
- <sup>9</sup>W. Hu, G. Z. Lum, M. Mastrangeli, and M. Sitti, Nature 554, 81 (2018).
- <sup>10</sup>V. E. Donohue, F. McDonald, and R. Evans, Journal of Applied Biomaterials 6, 69 (1995).
- <sup>11</sup>M. Suter, L. Zhang, E. C. Siringil, C. Peters, T. Luehmann, O. Ergeneman, K. E. Peyer, B. J. Nelson, and C. Hierold, Biomedical Microdevices 15, 997 (2013).
- <sup>12</sup>M. Sitti, H. Ceylan, W. Hu, J. Giltinan, M. Turan, S. Yim, and E. Diller, Proceedings of the IEEE 103, 205 (2015).
- <sup>13</sup>E. P. Furlani, in *Permanent Magnet and Electromechanical Devices*, Electromagnetism, edited by E. P. Furlani (Academic Press, San Diego, 2001) pp. 97–205.
- <sup>14</sup>J. J. Abbott, O. Ergeneman, M. P. Kummer, A. M. Hirt, and B. J. Nelson, IEEE Transactions on Robotics 23, 1247 (2007).
- <sup>15</sup>X. Wang, C. Hu, S. Pané, and B. J. Nelson, IEEE Robotics and Automation Letters 7, 1682 (2022).
- <sup>16</sup>D. P. Kingma and J. Ba, Adam: A Method for Stochastic Optimization (2017).
- <sup>17</sup>J. Lin, Z. Zhu, X. Jing, M. Lu, and Y. Gu, Advanced Theory and Simulations 4, 2100189 (2021).
- <sup>18</sup>L. Prades, S. Fabbri, A. D. Dorado, X. Gamisans, P. Stoodley, and C. Picioreanu, mBio 11, 10.1128/mbio.02813 (2020).

## Appendix A: Magnetic Field Validation

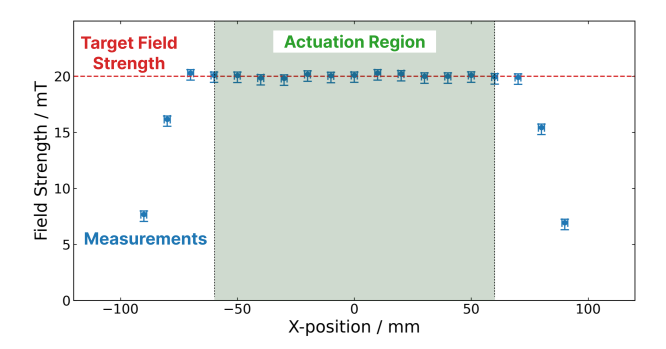
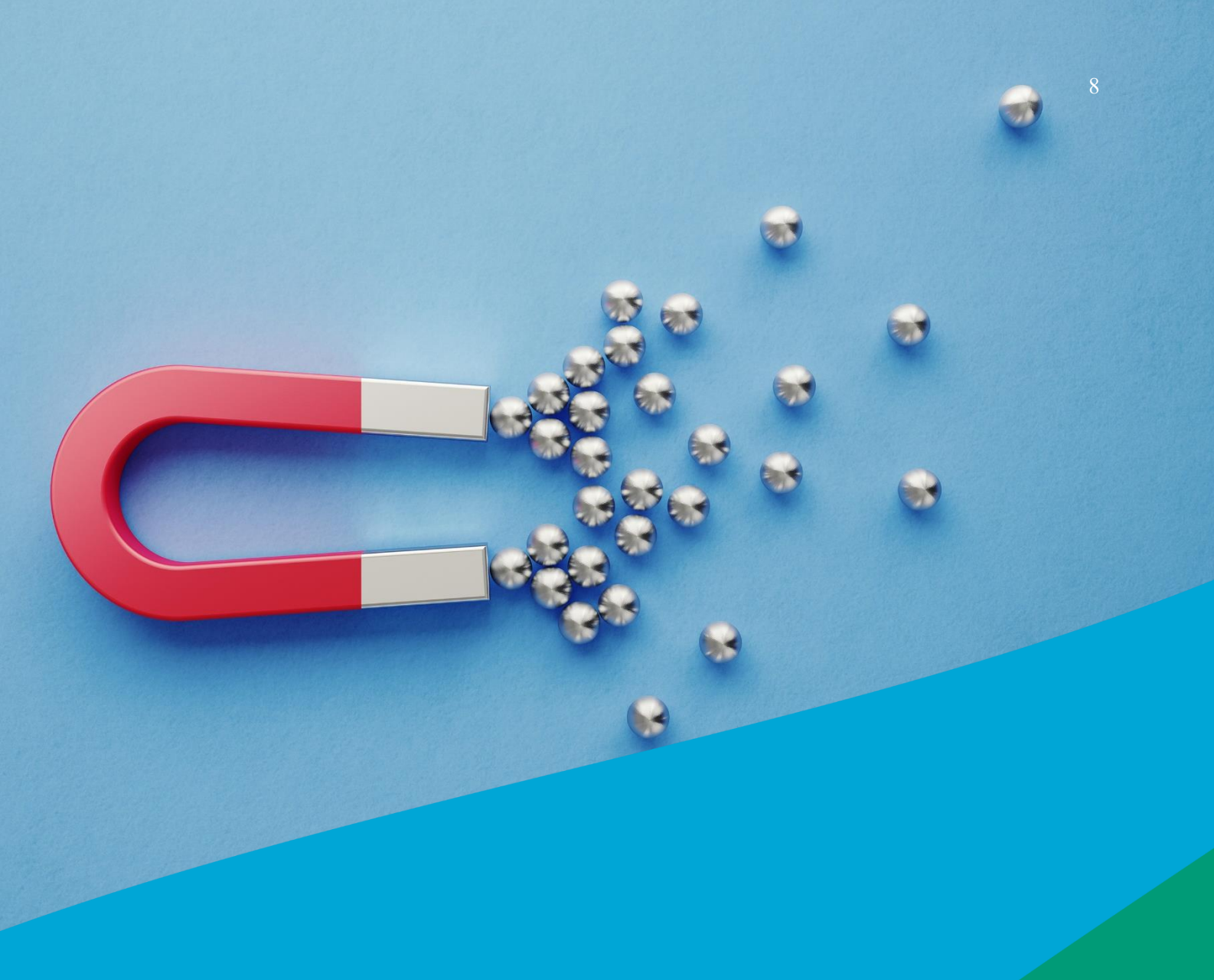


FIG. 6. Measured magnetic field strength along the central axis of the rotating magnetic field setup (x-axis). A  $20\,\mathrm{mT}$  field was maintained across the  $120\,\mathrm{mm}$  wide actuation region, with little deviation from the target field.



## Propulsion Performance Comparison of Hardand Soft-Magnetic Microrobots Under Rotating Magnetic Fields

**Supplementary Material 1: Magnetic Torque Calculations** 

Authors: Joost Wijnmaalen, Leon Abelmann, Iulian Apachitei

Dated: 11 July 2025



## **CONTENTS**

l.	Hard-Magnetic Torque	10
II.	Soft-Magnetic Torque	11
1	A. Unsaturated Soft-Magnetic Torque	11
E	B. Saturated Soft-Magnetic Torque	14
III.	. Torque Calculations Experiments	17
,	A. Torque Calculations Hard-Magnetic Experiments	17
E	B. Torque Calculations Soft-Magnetic Experiments	17
Ref	eferences	18

## I. HARD-MAGNETIC TORQUE

Magnetic torque describes the rotational force that acts on a magnetized object when exposed to an external magnetic field. It results from the tendency of the object's magnetization to align with the applied field and is given by<sup>1</sup>:

$$T = \mu_0 V M \times H_0 , \qquad (1)$$

where T is the torque vector,  $\mu_0$  is the permeability of free space, V is the volume of the magnetic body, M is the magnetization, and  $H_0$  is the applied magnetic field. For a diametrically magnetized hard-magnetic cylinder with an external magnetic field that is aligned with the radial axis of the cylinder (Fig. 1), Equation 1 simplifies to:

$$T = \mu_0 V M H_0 \sin \theta , \qquad (2)$$

where T is the total torque (around the x-axis), and  $\theta$  is the angle between the magnetization direction and the external magnetic field. This expression assumes uniform magnetization, a homogeneous external field, and ignores internal demagnetization effects.

Maximum magnetic torque is obtained when the magnetic field is perpendicular to the magnetization direction ( $\theta = 90^{\circ}$ ). Therefore, the maximum torque that hard magnets can generate is:

$$T_{max} = \mu_0 V M H_0 . \tag{3}$$

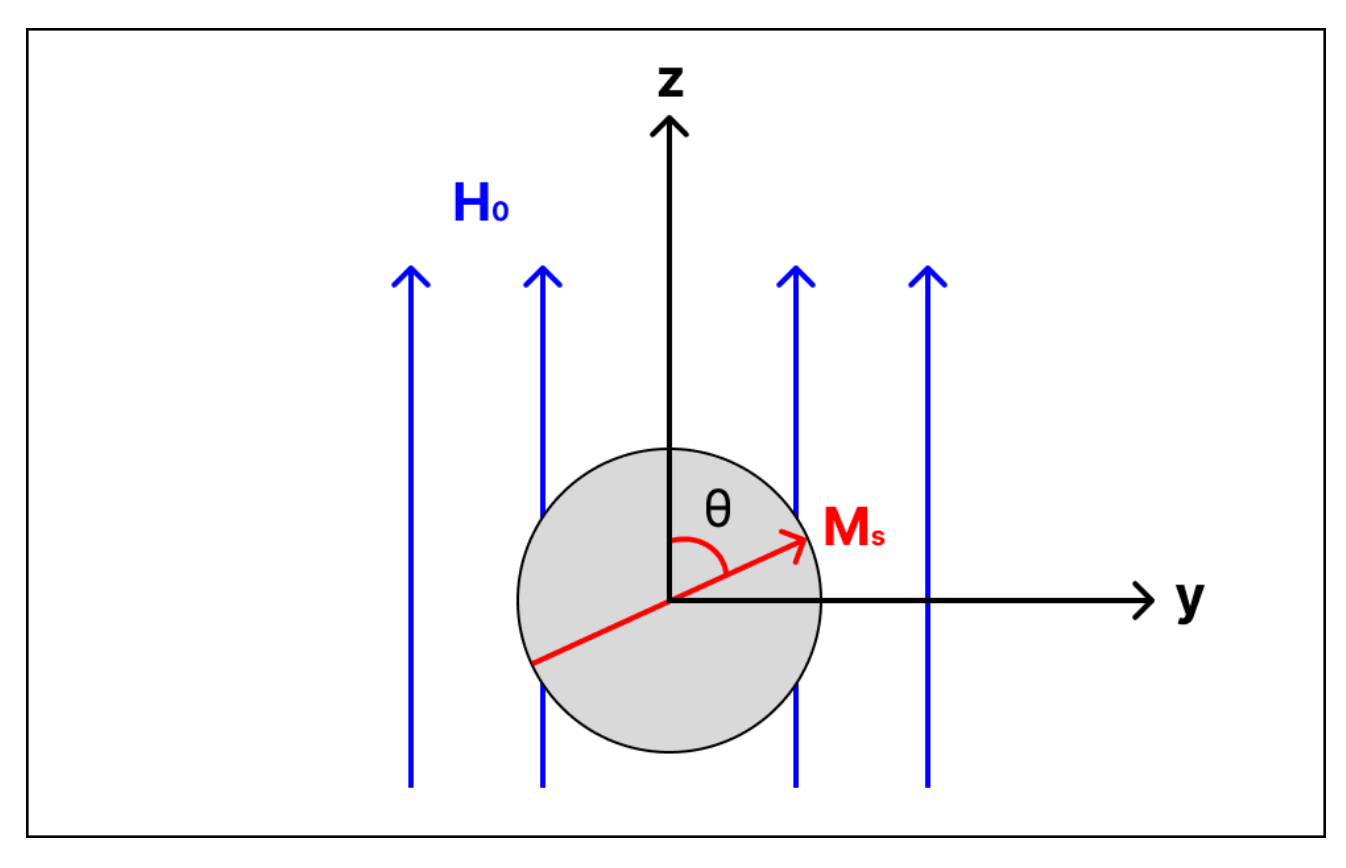


**Figure 1:** Diametrically magnetized hard-magnetic cylinder exposed to an external magnetic field applied in the radial (z-axis) direction.

## II. SOFT-MAGNETIC TORQUE

In soft-magnetic materials, shape anisotropy causes magnetization to align along a preferred geometric direction, known as the easy axis, to minimize internal magnetic energy. This concept can be illustrated using a one-dimensional rod composed of small magnetic domains. When an external magnetic field is applied perpendicular to the rod's long axis, like magnetic poles become positioned closely together (Fig. 2A), creating strong repulsive forces and increasing the internal magnetic energy. Conversely, aligning the rod parallel to the magnetic field separates the like poles (Fig. 2B), thereby reducing internal magnetic energy. To minimize magnetic energy, the soft-magnetic rod naturally aligns its long axis with the external magnetic field, generating torque. A practical demonstration is placing a sewing pin within an upward-oriented magnetic field (Fig. 2C), where it overcomes gravity and aligns vertically due to shape-anisotropic torque. Besides the volume of the magnetic material and the strength of the external magnetic field, the magnitude of the generated torque is determined by the demagnetization factor, which depends on the ratio between the rod's length and width, with higher torques observed in longer, thinner rods.

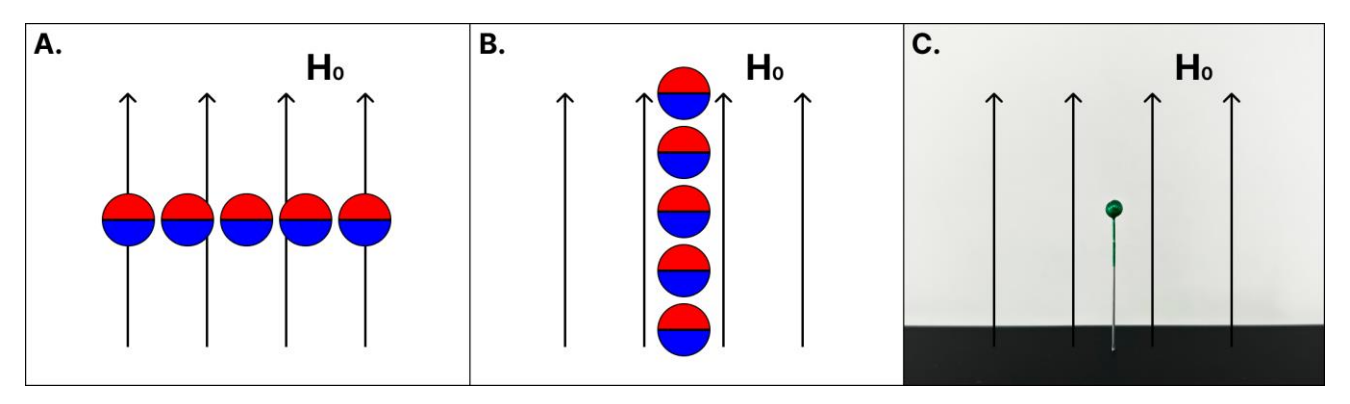


**Figure 2:** Working principles of shape anisotropy. **(A)** High internal magnetic energy when the rod is perpendicular to the field. **(B)** Low internal magnetic energy when the rod is parallel to the field. **(C)** Sewing pin overcoming gravity and aligning with the external magnetic field.

Before deriving the formulas for magnetic torque in soft magnets, several assumptions are made. The model assumes uniform magnetization, a uniform external magnetic field, linear magnetic response, absence of hysteresis effects, and high magnetic susceptibility ( $\chi >> 1$ ). Additionally, the demagnetization factors are based on the assumption of an ellipsoidal geometry. Furthermore, a coordinate system is used where the axial (long) axis is fixed. In this coordinate system, the internal magnetization and external magnetic field form angles  $\varphi$  and  $\theta$  with the fixed axial axis, respectively (Fig. 3A). Finally, it should be noted that there are two magnetization regions to consider: magnetization in the unsaturated region and magnetization in the saturated region<sup>2</sup>.

### A. Unsaturated Soft-Magnetic Torque

In the unsaturated region, the material's magnetization depends on the applied magnetic field  $H_0$  and the demagnetization factor N. Increasing the applied field strength raises the magnetization magnitude but does not affect the magnetization angle  $\varphi$ . As a result, angle  $\varphi$  can be fully expressed in terms of the applied field angle  $\theta$  and the demagnetization factor (Fig. 3B).

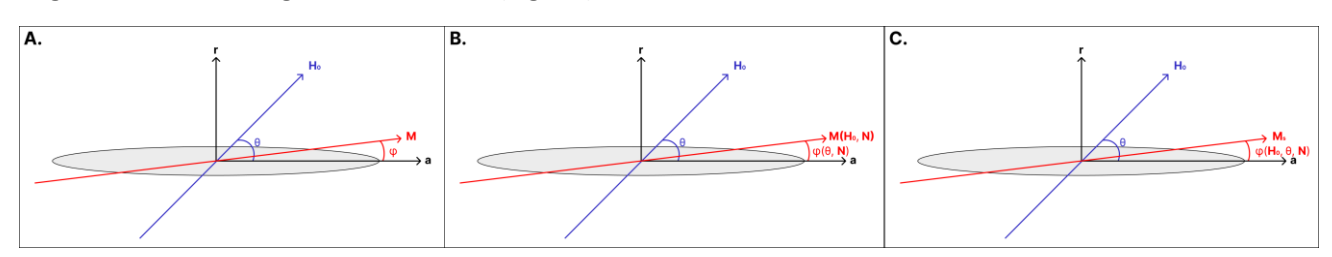


**Figure 3:** Magnetization under external fields. **(A)** Definition of the coordinate system and angles  $\varphi$  and  $\theta$ . **(B)** In the unsaturated regime, the magnitude of the magnetization increases with the external field strength  $H_0$ . The magnetization angle is set by the external field angle and the demagnetization factor N. **(C)** In the saturated regime, the magnetization magnitude remains constant at the saturation value. The magnetization angle depends on the external field strength, direction, and the demagnetization factor.

The torque in the unsaturated regime is derived by assuming a linear magnetization response, that is, the magnetization scales proportionally with the internal magnetic field:

$$M = \chi H_i$$
. (4)

Here,  $\chi$  denotes the magnetic susceptibility, which defines the proportionality between magnetization and the internal magnetic field. The internal magnetic field is obtained by combining the demagnetization field and the external magnetic field:

$$H_i = H_0 + H_d = H_0 - N \cdot M$$
, (5)

where N represents the demagnetization factor. Combining Equations 4 and 5 gives:

$$M = \chi_a H_0 . \tag{6}$$

Here,  $\chi_a$  denotes the apparent magnetic susceptibility, which accounts for the influence of the sample geometry, and is defined as:

$$\chi_{a} = \begin{bmatrix}
\frac{\chi}{1 + \chi n_{r}} & 0 & 0 \\
0 & \frac{\chi}{1 + \chi n_{a}} & 0 \\
0 & 0 & \frac{\chi}{1 + \chi n_{r}}
\end{bmatrix}, (7)$$

where  $n_a$  and  $n_r$  are the axial and radial demagnetization factors, respectively. Assuming high magnetic susceptibility, Equation 7 simplifies to:

$$\chi_{a} = \begin{bmatrix} \frac{1}{n_{r}} & 0 & 0\\ 0 & \frac{1}{n_{a}} & 0\\ 0 & 0 & \frac{1}{n_{r}} \end{bmatrix}. \tag{8}$$

 $H_0$  is given by:

$$\boldsymbol{H_0} = \begin{bmatrix} 0 \\ H_0 \cos \theta \\ H_0 \sin \theta \end{bmatrix}, \quad (9)$$

Therefore, combining Equations 6, 8, and 9 results in:

$$\mathbf{M} = \begin{bmatrix} 0 \\ \underline{H_0 \cos \theta} \\ n_a \\ \underline{H_0 \sin \theta} \\ n_r \end{bmatrix} . \tag{10}$$

Inserting Equations 9 and 10 into Equation 1 yields the torque in the unsaturated region:

$$T = \mu_0 V \begin{bmatrix} 0 \\ H_0 \cos \theta \\ n_a \\ H_0 \sin \theta \end{bmatrix} \times \begin{bmatrix} 0 \\ H_0 \cos \theta \\ H_0 \sin \theta \end{bmatrix} = \mu_0 V H_0^2 \cos \theta \sin \theta \left( \frac{1}{n_a} - \frac{1}{n_r} \right) = \frac{\mu_0 V H_0^2 (n_r - n_a)}{2n_a n_r} \sin 2\theta \, \hat{\mathbf{e}}_{\perp} \,. \tag{11}$$

The magnitude of the torque simplifies to:

$$|T| = \frac{\mu_0 V H_0^2 (n_r - n_a)}{2n_a n_r} \sin 2\theta .$$
 (12)

The torque reaches its maximum when  $\theta = 45^{\circ}$ :

$$|T_{max}| = |T(\theta = 45^{\circ})| = \frac{\mu_0 V H_0^2 (n_r - n_a)}{2n_a n_r}.$$
 (13)

Demagnetization factor  $n_a$  can be calculated with<sup>3</sup>:

$$n_a = \frac{1}{R^2 - 1} \left( \frac{R}{2\sqrt{R^2 - 1}} \ln \left( \frac{R + \sqrt{R^2 - 1}}{R - \sqrt{R^2 - 1}} \right) - 1 \right), \quad (14)$$

where R is the ratio between the axial and radial dimensions.  $n_r$  can be calculated with:

$$n_r = \frac{1 - n_a}{2} \,. \tag{15}$$

In conclusion, for an axially symmetric soft-magnetic body in the unsaturated regime, torque arises from the competition between shape anisotropy, which confines the magnetization near the symmetry axis, and the transverse component of the external field, which tends to rotate the magnetization away from this axis. A field applied at 45° provides the optimal balance between magnetization and transverse field strength, resulting in maximum torque.

When the applied magnetic field becomes sufficiently strong to saturate the magnetic body, additional field strength no longer increases internal magnetization. Instead, it rotates the magnetization vector toward the direction of the external field. As a result, keeping the external field at 45° no longer yields maximum torque since the transverse component diminishes as the magnetization aligns with the field. To maximize the torque, the external field must be applied at an angle greater than 45°. This necessitates a different approach to calculate the maximum torque. Therefore, Equation 13 remains valid only if:

$$H_0 < H_{sat}(45^\circ)$$
. (16)

The saturation field  $H_{sat}$  can be determined by inserting the saturation magnetization  $M_s$  and  $H_{sat}$  in Equation 6, yielding:

$$M_s = \sqrt{\left(\frac{H_{sat}\cos\theta}{n_a}\right)^2 + \left(\frac{H_{sat}\sin\theta}{n_r}\right)^2} \ . \tag{17}$$

Solving for  $H_{sat}$  results in the general expression for the saturation field:

$$H_{sat}(\theta) = M_s \frac{n_a n_r}{\sqrt{n_a^2 \sin^2 \theta + n_r^2 \cos^2 \theta}} \,. \tag{18}$$

For the special case where the applied field is oriented at  $\theta=45^{\circ}$ , this simplifies to:

$$H_{sat}(45^{\circ}) = H_{low} = \frac{M_s n_a n_r \sqrt{2}}{\sqrt{n_a^2 + n_r^2}} \,.$$
 (19)

### **B. Saturated Soft-Magnetic Torque**

Once a soft-magnetic rod is fully saturated, further increases in the external field do not increase the magnetization magnitude but instead rotate its direction toward that of the external field. The final orientation of the magnetization minimizes the total magnetic energy, which consists of two competing contributions: the demagnetization (shape anisotropy) energy, which favors alignment along the rod's long axis, and the Zeeman energy, which favors alignment with the external field. The balance between these energies determines how far the magnetization tilts toward the external field. Consequently, the magnetization angle now depends on the external field's direction, its strength, and the demagnetization factor, whereas the magnitude of the magnetization remains fixed (Fig. 3C). In powerful fields, this process drives the magnetization to lie almost exactly along the applied field despite the material's geometric preference.

In the saturated region, the magnetization is determined solely by the saturation magnetization of the material and can be expressed as:

$$\mathbf{M} = \begin{bmatrix} 0 \\ M_s \cos \varphi \\ M_s \sin \varphi \end{bmatrix}. \tag{20}$$

Consequently, Equation 1 becomes:

$$\mathbf{T} = \mu_0 V M_s H_0 \sin(\theta - \varphi) \,\hat{\mathbf{e}}_{\perp} \,. \tag{21}$$

Which simplifies to:

$$|T| = \mu_0 V M_s H_0 \sin(\theta - \varphi) . \qquad (22)$$

To evaluate the torque as a function of the applied field angle  $\theta$  and field strength  $H_0$ , the magnetization angle  $\varphi$  must first be determined. This angle follows from minimizing the total magnetic energy  $E_{mag}$ , where  $\varphi$  depends on the balance between the demagnetization and Zeeman terms for a given external field. The total magnetic energy can be expressed as:

$$E_{mag} = E_{demag} + E_{zeeman}. (23)$$

With:

$$E_{demag} = -\frac{1}{2}\mu_0 \int \mathbf{M} \cdot \mathbf{H} dV = -\frac{1}{2}\mu_0 V \mathbf{M} \cdot \mathbf{H}_{demag} = \frac{1}{2}\mu_0 V \mathbf{M}^T \mathbf{N} \mathbf{M}$$

$$E_{ext} = -\mu_0 \int \mathbf{M} \cdot \mathbf{H}_{ext} dV = -\mu_0 V \mathbf{M} \cdot \mathbf{H}_{\mathbf{0}} .$$
(24)

Combining Equations 22-25 yields:

$$E_{mag} = \frac{1}{2}\mu_0 V(n_r - n_a) M_s^2 \sin^2 \varphi - \mu_0 V M_s H_0 \cos(\theta - \varphi) . \tag{26}$$

The magnetization angle is obtained by minimizing the total energy, which is done by setting its first derivative with respect to  $\varphi$  equal to zero:

$$\frac{d}{d\varphi}E_{mag} = 0 \to (n_r - n_a)M_s \sin 2\varphi = 2H_0 \sin(\theta - \varphi) . \tag{27}$$

Substituting this equilibrium value of  $\varphi$  into Equation 22 yields:

$$|T| = \frac{1}{2}\mu_0 V(n_r - n_a) M_s^2 \sin 2\varphi$$
 (28)

The maximum torque is obtained when  $\varphi$  equals 45°:

$$|T_{max}| = |T(\varphi = 45^{\circ})| = \frac{1}{2}\mu_0 V(n_r - n_a) M_s^2$$
. (29)

Maximum torque can only be reached when the external magnetic field is strong enough to deflect the (saturated) magnetization by 45° from the long axis. The minimal strength of the external field that can rotate the saturated magnetization vector to 45° is denoted as  $H_{high}$ . This value can be determined by combining the energy equilibrium equation (Equation 27) with the condition that  $H_{high}$  corresponds to the minimal field strength required to achieve saturation at  $\varphi=45^\circ$ . In this condition, the system is still at the upper bound of the linear domain. Therefore, the relation between the applied field angle  $\theta$  and the magnetization angle  $\varphi$  can be calculated with Equation 6 as:

$$\varphi = \tan^{-1} \frac{M_r}{M_a} = \tan^{-1} \frac{n_a}{n_r} \frac{H_{0r}}{H_{0a}} = \tan^{-1} \left( \frac{n_a}{n_r} \tan \theta \right).$$
 (30)

Inserting  $\theta_{opt}$  results in:

$$\tan \varphi = \frac{n_a}{n_r} \tan \theta_{opt} \ . \tag{31}$$

Setting  $\varphi = 45$  ° gives the corresponding optimal applied field angle:

$$\theta_{opt} = tan^{-1} \frac{n_r}{n_a} \,. \tag{32}$$

Inserting  $\theta_{opt}$  into the equilibrium equation (Equation 27) yields:

$$(n_r - n_a)M_s \sin 2\varphi = 2H_{high} \sin(\theta_{opt} - \varphi). \tag{33}$$

Combining equations 32 and 33 and setting  $\varphi = 45^{\circ}$  results in:

$$H_{high} = M_s \sqrt{\frac{n_a^2 + n_r^2}{2}} \,. \tag{34}$$

For intermediate field strengths ( $H_{low} \leq H \leq H_{high}$ ), saturation magnetization is reached when the magnetic field is applied at an angle of 45°. However, this intermediate field strength is not sufficient to rotate the internal (saturated) magnetization to 45°. In this case, the highest possible torque occurs when the magnetization magnitude is maximized and the angle between  $\theta$  and  $\varphi$  is as large as possible. This condition is met when  $\theta$  is such that the saturation magnetization is just reached. Increasing the field strength further at the same angle would rotate the magnetization vector towards the applied magnetic field direction without increasing its magnitude, thereby reducing the torque. Therefore, inserting  $\theta_{opt}$  in Equation 18 results in:

$$\tan \theta_{opt} = \frac{nr}{na} \sqrt{\frac{H_0^2 - M_s^2 n_a^2}{M_s^2 n_r^2 - H_0^2}}.$$
 (35)

Inserting Equation 35 in Equation 31 gives:

$$\tan \varphi = \sqrt{\frac{H_0^2 - M_s^2 n_a^2}{M_s^2 n_r^2 - H_0^2}}.$$
 (36)

Now, the  $\sin 2\varphi$  component from the equilibrium relation (Equation 27) can be expressed as:

$$\sin 2\varphi = \frac{2\tan\varphi}{1+\tan^2\varphi} = \frac{2\sqrt{(M_s^2n_a^2 - H_0^2)(H_0^2 - M_s^2n_r^2)}}{M_s^2(n_r - n_a)(n_r + n_a)}.$$
 (37)

Therefore, the torque from Equation 28 becomes:

$$|\mathbf{T}| = \frac{\mu_0 V}{n_r + n_a} \sqrt{(M_s^2 n_a^2 - H_0^2)(H_0^2 - M_s^2 n_r^2)}.$$
 (38)

In conclusion, there are three distinct maximum torques for three different magnetization regions: an unsaturated region ( $H_0 \le H_{low}$ ), an intermediate saturated region where the magnetization angle cannot be brought to 45° ( $H_{low} \le H_0 \le H_{high}$ ), and a saturated region where the magnetization angle can reach 45° ( $H_0 \ge H_{high}$ ):

$$T_{max} = \begin{cases} \frac{\mu_0 V H_0^2 \ (n_r - n_a)}{2n_a n_r}, \ H_0 \le H_{low}, \ \theta_{opt} = 45^{\circ} \\ \frac{\mu_0 V}{n_r + n_a} \sqrt{\left(M_s^2 n_a^2 - H_0^2\right) \left(H_0^2 - M_s^2 n_r^2\right)}, \ H_{low} \le H_0 \le H_{high}, \ \theta_{opt} = tan^{-1} \left(\frac{nr}{na} \sqrt{\frac{H_0^2 - M_s^2 n_a^2}{M_s^2 n_r^2 - H_0^2}}\right) \\ \frac{\mu_0 V M_s^2 \ (n_r - n_a)}{2}, H_0 \ge H_{high}, \theta_{opt} = sin^{-1} \left(\frac{M_s \ (n_r - n_a)}{2H}\right) + 45^{\circ}. \end{cases}$$

$$(39)$$

Interestingly, this means that the generated torque is independent of the applied magnetic field beyond  $H_{high}$ , and the absolute maximum torque is achieved when  $\phi$  = 45°. Increasing  $H_0$  past  $H_{high}$  will only decrease the optimal angle  $\theta_{opt}$  towards 45°, without increasing torque.

## III. TORQUE CALCULATIONS EXPERIMENTS

## A. Torque Calculations Hard-Magnetic Experiments

The hard-magnetic microrobots used in the experiments contained a cylindrical NdFeB magnet (N42; first4magnets, Sutton-in-Ashfield, United Kingdom) with a diameter of 1 mm and a length of 3 mm. This results in a volume of  $2.36 \text{ mm}^3$  and a remanent magnetization M of 1.03 MA/m (1.3 T). Together with an external magnetic field of 15.9 kA/m (20 mT), Equation 3 becomes:

$$T_{mgr}^{NdFeB} = 4\pi * 10^{-7} * 2.36 * 10^{-9} * 1.03 * 10^{6} * 15.9 * 10^{3} = 48.6 \,\mu\text{Nm}$$
.

## **B. Torque Calculations Soft-Magnetic Experiments**

The soft-magnetic microrobots contained either ferrite (78 material; Fair-Rite, Wallkill, United States) or pure Fe (99.5% purity; Goodfellow, Huntingdon, United Kingdom), both with a diameter of 0.75 mm and a length of 5.33 mm to match the magnetic volume of the hard-magnetic microrobots. Therefore, the ratio between the axial and radial direction *R* is 7.11. Inserting this ratio in Equation 14 yields:

$$n_a = \frac{1}{7.11^2 - 1} \left( \frac{7.11}{2\sqrt{7.11^2 - 1}} \ln \left( \frac{7.11 + \sqrt{7.11^2 - 1}}{7.11 - \sqrt{7.11^2 - 1}} \right) - 1 \right) = 0.034.$$

Inserting  $n_a$  into Equation 15 results in:

$$n_r = \frac{1 - 0.034}{2} = 0.483$$
.

Ferrite and pure Fe have saturation magnetizations of 0.38 MA/m (0.48 T) and 1.43 MA/m (1.8 T), respectively. The applied magnetic field at which saturation is reached is calculated by Equation 19:

$$H_{low}^{ferrite} = \frac{0.38 * 10^6 * 0.034 * 0.483 * \sqrt{2}}{\sqrt{0.034^2 + 0.483^2}} = 18.2 \ kA/m$$

$$H_{low}^{pure \, Fe} = \frac{1.43 * 10^6 * 0.034 * 0.483 * \sqrt{2}}{\sqrt{0.034^2 + 0.483^2}} = 68.6 \, kA/m \,.$$

This indicates that neither magnetic material will be saturated by an external magnetic field of 15.9 kA/m (20 mT), and therefore, Equation 13 can be used to determine the maximum torque. As Equation 13 does not depend on magnetic susceptibility, the torque is the same for both materials:

$$T_{max} = \frac{4\pi * 10^{-7} * 2.36 * 10^{-9} * (15.9 * 10^{3})^{2} * (0.483 - 0.034)}{2 * 0.034 * 0.483} = 10.24 \,\mu\text{Nm} \,.$$

This indicates the expected magnetic torque for hard-magnetic materials is approximately 4.7 times higher.

## **REFERENCES**

- <sup>1</sup>E. P. Furlani, in *Permanent Magnet and Electromechanical Devices*, Electromagnetism, edited by E. P. Furlani (Academic Press, San Diego, 2001) pp. 97–205.
- <sup>2</sup>J. J. Abbott, O. Ergeneman, M. P. Kummer, A. M. Hirt, and B. J. Nelson, IEEE Transactions on Robotics **23**, 1247 (2007).
- <sup>3</sup>J. A. Osborn, Physical Review **67**, 351 (1945).



## Propulsion Performance Comparison of Hardand Soft-Magnetic Microrobots Under Rotating Magnetic Fields

Supplementary Material 2: Magnetic Array Optimization

Authors: Joost Wijnmaalen, Leon Abelmann, Iulian Apachitei

Dated: 11 July 2025



## **CONTENTS**

I.	Introduction	21
II.	Theory	22
Α	. Computational Acceleration	22
В	. Magnetic Field	22
С	. Optimization Algorithms	24
III.	Results and Discussion	28
Α	. Preliminary Evaluation of Magnet Configurations	28
В	. Magnet Array Optimization	32
С	. Constructed Magnetic Array	36
IV.	Conclusions	37
٧.	Experimental	38
Α	. Computational Setup	38
В	. Magnet Characteristics	38
С	. Array Fabrication	38
D	. Magnetic Field Validation	39
Ref	erences	40
A. S	tep Function Optimization	41
B. S	caled Optimization Performance	42

## I. INTRODUCTION

Magnetic microrobots are commonly actuated using tri-axial Helmholtz coil setups, which consist of three orthogonal pairs of opposing coils. By independently controlling the current through each coil, these systems generate highly uniform rotating magnetic fields, enabling precise control and accurate characterization of microrobots. However, such systems are expensive, often exceeding \$20,000<sup>1</sup>.

A lower-cost alternative involves the use of rotating permanent magnets. These setups, however, typically rely on a single magnet, resulting in non-uniform fields with poorly defined strengths that hinder reliable microrobot characterization<sup>2</sup>.

This Supplemental Material describes the design of two opposing permanent-magnet arrays capable of generating uniform magnetic fields at specific field strengths by using a multivariate optimization algorithm. The requirements for these arrays are:

- A 20 mT magnetic field strength, the upper bound of off-the-shelf tri-axial Helmholtz coil setups.
- A maximum deviation of 0.5 mT from the target field, ensuring that actuation is primarily governed by magnetic torque rather than gradient-induced forces.
- A 120 mm region of 20 mT field strength, allowing the 10 mm microrobot to be propelled over a 100 mm distance, which provides a good balance between fabrication feasibility and characterization length.
- A minimum spacing of 30 mm between the magnetic arrays, providing sufficient clearance for the microrobots to move freely between them.
- A maximum array size of 250 mm, remaining within the fabrication limits of conventional 3D-printing systems.

The design of these magnetic arrays is detailed across four sections: Theory (Chapter 2), Results & Discussion (Chapter 3), Conclusion (Chapter 4), and Experimental (Chapter 5). The Python code for optimization and the 3D model of the magnetic array are available on GitHub.

## II. THEORY

## A. Computational Acceleration

All calculations were performed using Python's JAX library. JAX is a high-performance numerical computing library developed by Google, especially suited for machine learning and scientific computing. A core feature of JAX is Just-In-Time (JIT) compilation. When a function is JIT-compiled, JAX traces the function the first time it is called with a set of inputs. During this tracing phase, JAX records all operations in a computational graph using an intermediate representation called XLA (Accelerated Linear Algebra). This graph is then compiled into optimized machine code tailored to the target hardware (CPU, GPU, or TPU). The compilation significantly reduces Python overhead and enables fused and vectorized operations, which can drastically speed up computation, especially for large-scale numerical workloads. After compilation, the compiled version of the function is cached and reused for subsequent calls with the same input shapes and types, providing fast execution without re-tracing. However, if the input shapes or data types change, JAX recompiles the function, which can introduce overhead. Therefore, JIT compilation in JAX is most effective when input shapes are consistent across calls.

Another key feature of JAX is automatic differentiation. JAX uses reverse-mode automatic differentiation (autograd) to trace operations and compute exact gradients by reusing intermediate computations, which is significantly faster and more accurate than finite-difference methods<sup>3</sup>.

## **B.** Magnetic Field

The theoretical model for the magnetic field was derived from the surface charge model. In the surface-charge model, the magnetic field generated by a magnetized object is represented by an equivalent distribution of magnetic surface charges. For a uniformly magnetized rectangular bar, the surface charge density is<sup>4</sup>:

$$\sigma_m = M * \widehat{n}$$
, (1)

where M is the magnetization and  $\hat{n}$  the outward unit normal vector at the magnet's surface. The field at a specific point r due to an infinitesimal patch of surface charge  $\sigma_m$  at location r' is:

$$dB(r) = \frac{\mu_0}{4\pi} \sigma_m \frac{r - r'}{\|r - r'\|^3} dS, \quad (2)$$

where dB(r) describes the infinitesimal contribution to the magnetic field at an observation point r due to surface element dS carrying a magnetic surface charge density  $\sigma_m$ .  $\mu_0$  accounts for the free-space permeability and  $\frac{r-r'}{\|r-r'\|^3}$  represents the field contribution from a surface charge located at r', where  $\|r-r'\|$  is the Euclidean distance between the source and observation point.

The total magnetic field at a given point is obtained by evaluating the surface integral over all infinitesimal surface charge elements:

$$\boldsymbol{B}(\boldsymbol{r}) = \frac{\mu_0}{4\pi} \oint_{S} \boldsymbol{\sigma_m} \frac{\boldsymbol{r} - \boldsymbol{r}'}{\|\boldsymbol{r} - \boldsymbol{r}'\|^3} dS.$$
 (3)

For a block magnet, this leads to the evaluation of a double integral over a square surface element dS = dx dy for each Cartesian field component. Since the block magnet has a flat surface located at constant height z', it follows that:

$$B_{x} = \frac{\mu_{0}}{4\pi} M_{x} \int_{a}^{b} \int_{c}^{d} \frac{x - x'}{((x - x')^{2} + (y - y')^{2} + z^{2})^{\frac{3}{2}}} dy' dx'$$
 (4)

$$B_{y} = \frac{\mu_{0}}{4\pi} M_{y} \int_{a}^{b} \int_{c}^{d} \frac{y - y'}{((x - x')^{2} + (y - y')^{2} + z^{2})^{\frac{3}{2}}} dy' dx'$$
 (5)

$$B_z = \frac{\mu_0}{4\pi} M_z \int_a^b \int_c^d \frac{z}{((x-x')^2 + (y-y')^2 + z^2)^{\frac{3}{2}}} dy' dx', \qquad (6)$$

where a and b are the bounds of the magnet in the x-direction, and c and d are the bounds in the y-direction. These integrals are subsequently solved using Gauss-Legendre quadrature<sup>5</sup>. Gauss-Legendre quadrature approximates the integral of the form:

$$I = \int_{-1}^{1} f(x)dx , \qquad (7)$$

by evaluating the function at specific points (nodes) within the interval [-1, 1] and weighting them:

$$I \approx \sum_{i=1}^{n} w_i f(x_i) , \qquad (8)$$

where  $x_i$  are the nodes and  $w_i$  are the corresponding weights. The chosen nodes and weights are not evenly spaced, as in Riemann sums, but are located at Gauss points. Gauss points are determined by the roots of the Legendre polynomials, which are defined recursively as<sup>6</sup>:

$$P_0(x) = 1 (9)$$

$$P_1(x) = x (10)$$

$$P_{n+1}(x) = \frac{2n+1}{n+1} x P_n(x) - \frac{n}{n+1} P_{n-1}(x) . (11)$$

The corresponding weights are given by:

$$w_i = \frac{2}{(1 - x_i^2)[P'_n(x_i)]^2}, \quad (12)$$

where P' denotes the derivative of the Legendre polynomial at  $x_i$ . For a block magnet, the integral is defined over an arbitrary interval [a, b], rather than [-1, 1]. To apply Gauss-Legendre quadrature, the integration domain [a, b] is mapped to [-1, 1] using the transformation:

$$x = \frac{b - a}{2}\xi + \frac{b + a}{2}, \quad (13)$$

where  $\xi$  is the transformed integration variable running from -1 to 1 after mapping the original interval [a, b] to the standard domain for Gauss-Legendre quadrature. Equation 13 transforms the integral into the following form:

$$\int_{a}^{b} f(x)dx = \frac{b-a}{2} \int_{-1}^{1} f\left(\frac{b-a}{2}\xi + \frac{b+a}{2}\right) d\xi.$$
 (14)

Subsequently, Equation 8 becomes:

$$\int_{a}^{b} f(x)dx \approx \sum_{i=1}^{n} w_{i} f\left(\frac{b-a}{2}x_{i} + \frac{b+a}{2}\right). \tag{15}$$

For surface integrals, Equation 15 can be extended to:

$$\int_{a}^{b} \int_{c}^{d} f(x,y)dydx = \frac{(b-a)(c-d)}{4} \sum_{i=1}^{n} \sum_{j=1}^{n} w_{i}w_{j}f\left(\frac{b-a}{2}x_{i} + \frac{b+a}{2}, \frac{d-c}{2}x_{j} + \frac{d+c}{2}\right), \quad (16)$$

where  $x_i$  and  $w_i$  are nodes and weights corresponding to the integration along the x-axis over the interval [a, b], and  $x_i$  and  $w_i$  are the nodes and weights corresponding to the integration along the y-axis over the interval [c, d]. Overall, Gauss-Legendre quadrature significantly improves accuracy compared to other numerical integration methods. Moreover, a fixed set of nodes and weights can be used for any integration bounds, making the quadrature highly suitable for JIT-compilation, resulting in a substantial speedup.

The magnetic gradient is subsequently calculated by evaluating the spatial derivatives of the magnetic field:

$$\nabla \mathbf{B} = \left(\frac{\partial B}{\partial x}, \frac{\partial B}{\partial y}, \frac{\partial B}{\partial z}\right). \tag{17}$$

The calculations of Equation 17 are performed through the automatic differentiation of JAX.

## C. Optimization Algorithms

Five multivariate optimization algorithms were evaluated: grid search, hierarchical optimization, the Limited-memory Broyden-Fletcher-Goldfarb-Shanno algorithm (L-BFGS), multistart L-BFGS, and the Adaptive Moment Estimation algorithm (Adam). Each optimization algorithm aims to determine the parameter combination that produces a magnetic field as close as possible to the target value across a set of observation points. To quantify the mismatch, the squared error between the computed and target magnetic field is used as the objective function:

$$E = \sum_{k=1}^{n} (B_k - B_{REF})^2, \quad (18)$$

where  $B_k$  is the computed field at observation point k and  $B_{REF}$  is the target magnetic field.

## **Grid Search**

Grid search minimizes the objective function by exhaustively evaluating all possible parameter combinations<sup>7</sup>. The search space is defined as the Cartesian product of the sampled parameter values:

$$\mathbf{x} \in \mathcal{G} = \left\{ x_1^{(i_1)}, x_2^{(i_2)}, \dots, x_n^{(i_n)} \right\},$$
 (19)

where  $i_n$  indexes the sampled value of parameter  $x_n$ . The parameter set yielding the lowest error is selected as the optimal solution:

$$\mathbf{x}^* = \arg\min_{\mathbf{x} \in \mathcal{G}} f(\mathbf{x}) . \qquad (20)$$

## **Hierarchical Optimization**

Hierarchical optimization minimizes the objective function by iteratively refining the parameter space<sup>8</sup>. Starting with an initial coarse grid search, it zooms in on the parameter combination that yields the lowest error. Subsequently, a local grid search is performed. For each independent parameter, a small discrete interval is constructed by selecting three candidate values: the current parameter value, as well as values offset by  $\pm \frac{1}{2}$  of the previous step size:

$$x_j \in \left\{ x_j^* - \frac{\Delta}{2}, x_j^*, x_j^* + \frac{\Delta}{2} \right\}.$$
 (21)

The procedure repeats, halving the step size after each iteration, and therefore requires fewer evaluations than grid search, which evaluates the entire design space.

## Limited-Memory Broyden-Fletcher-Goldfarb-Shanno Algorithm

The L-BFGS algorithm is a second-order gradient-based optimization method that iteratively estimates the curvature of the objective function at different parameter combinations<sup>9</sup>. In standard gradient descent, the parameters are updated by moving in the direction of steepest decrease, as indicated by a negative gradient.

Since the gradient describes how the function changes at a given point, following its negative direction locally reduces the objective function most effectively. At each iteration, k, the parameters are updated according to:

$$\mathbf{x}_{k+1} = \mathbf{x}_k - \alpha \nabla f(\mathbf{x}_k) \,, \qquad (22)$$

where  $\alpha$  is the step size. However, gradient descent uses only local gradient information and does not account for the curvature of the objective function, limiting its efficiency. Second-order methods address this by using curvature information contained in the Hessian matrix of the objective function to adjust the search direction and step size. Since computing the full Hessian is computationally intensive, L-BFGS approximates the Hessian by incorporating information from previous iterations. Specifically, it stores differences between consecutive parameter vectors and gradients:

$$\mathbf{s}_k = \mathbf{x}_{k+1} - \mathbf{x}_k \tag{23}$$

$$\mathbf{y}_k = \nabla f(\mathbf{x}_{k+1}) - \nabla f(\mathbf{x}_k) \,. \tag{24}$$

Here,  $s_k$  represents the change in the parameter vector between two consecutive iterations, and  $y_k$  the corresponding change in the gradient. These differences capture how the slope of the objective function evolves as the parameters are updated, thereby providing indirect information about the function's local curvature. Liu *et al.* demonstrated that this information can be used to approximate the Hessian<sup>9</sup>. The parameters are now updated according to:

$$\mathbf{x}_{k+1} = \mathbf{x}_k - \alpha_k \mathbf{H}_k \nabla f(\mathbf{x}_k) \,, \quad (25)$$

where  $H_k$  is the approximation of the inverse Hessian and  $\alpha_k$  is the new step size. Equation 25 can be simplified to:

$$\boldsymbol{x}_{k+1} = \boldsymbol{x}_k + \alpha_k \boldsymbol{p}_k \,, \quad (26)$$

where step size  $\alpha_k$  is determined by satisfying the Wolfe conditions. The Wolfe conditions impose two requirements. First, the sufficient decrease condition ensures that the step results in an adequate reduction of the objective function relative to the decrease predicted by the current gradient:

$$f(\boldsymbol{x}_k + \alpha_k \boldsymbol{p}_k) \le f(\boldsymbol{x}_k) + c_1 \alpha_k \nabla f(\boldsymbol{x}_k)^T \boldsymbol{p}_k , \quad (27)$$

where  $c_1$ , typically set to  $10^{-4}$ , is the constant that determines how much decrease in the objective function is required for the step size to be accepted. The second requirement is the curvature condition, which verifies that the slope of the function along the search direction is sufficiently reduced after taking the step. This condition is given by:

$$\nabla f(\boldsymbol{x}_k + \alpha_k \boldsymbol{p}_k)^T \boldsymbol{p}_k \ge c_2 \nabla f(\boldsymbol{x}_k)^T \boldsymbol{p}_k , \qquad (28)$$

where  $c_2$ , typically set to 0.9, determines the acceptable change in slope. The L-BFGS algorithm performs a line search where the step size  $\alpha_k$  is decreased until both Wolfe conditions are satisfied.

L-BFGS and other advanced optimization algorithms operate by evaluating the numerical values of parameters over the entire real line  $[-\infty, \infty]$ . However, in certain applications, such as the placement of magnets, the parameters are subject to specific constraints (see Chapter 1). To enforce these bounds on the independent variables, the sigmoid function can be utilized. The sigmoid function is defined as:

$$\sigma(u) = \frac{1}{1 + e^{-u}} , \qquad (29)$$

where u is the unbounded optimization variable, and  $\sigma(u)$  maps u to the interval [0, 1]. To map this bounded output to the desired range [a, b], a transformation needs to be applied:

$$x = a + (b - a)\sigma(u). \tag{30}$$

Here, x is the transformed variable, now bounded between a and b.

L-BFGS determines its search direction based on the gradient and curvature near the current parameter values. When the objective function contains multiple minima, the algorithm can become trapped in a local minimum if it starts in a region that leads to that minimum. Since L-BFGS does not explore the entire parameter space but follows the local slope, it may converge to a solution that reduces the error locally but does not reach the global minimum (Fig. 1).

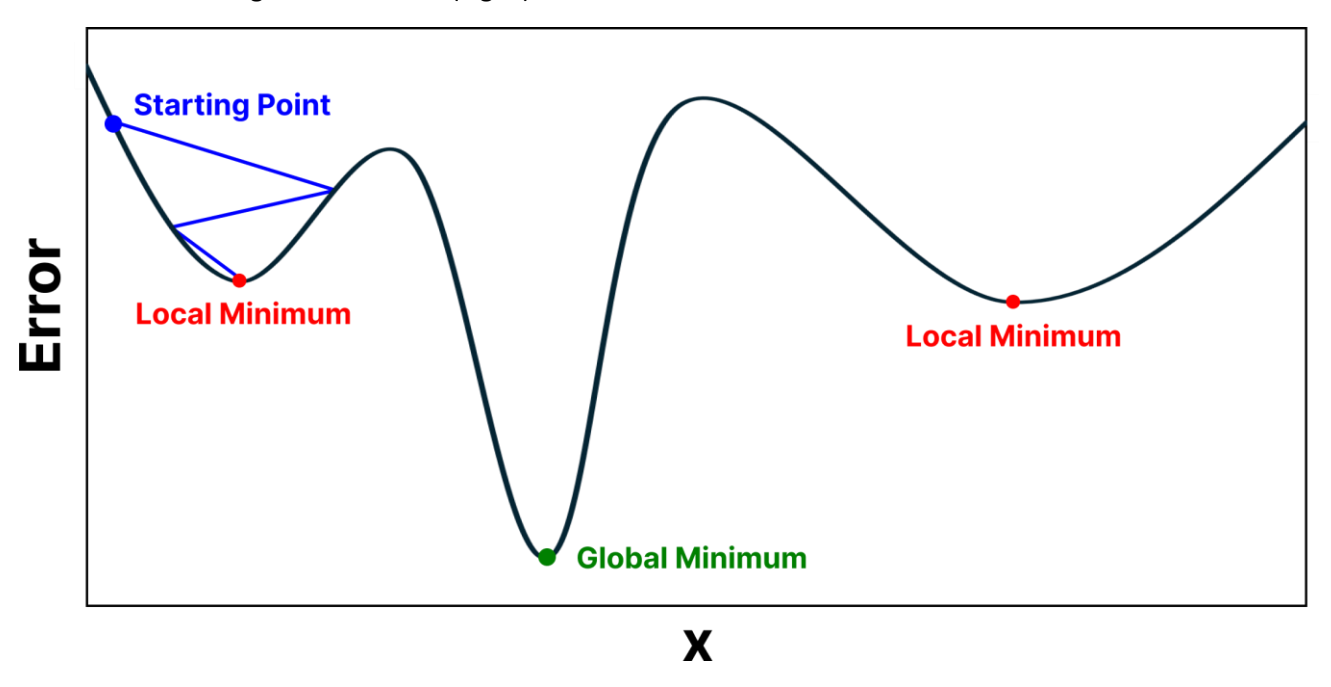


Figure 1: Convergence to a local minimum instead of the global minimum depending on the choice of starting point.

This problem is addressed by multistart L-BFGS, which explores multiple starting points in parallel and can therefore converge to the global minimum (Fig. 2).

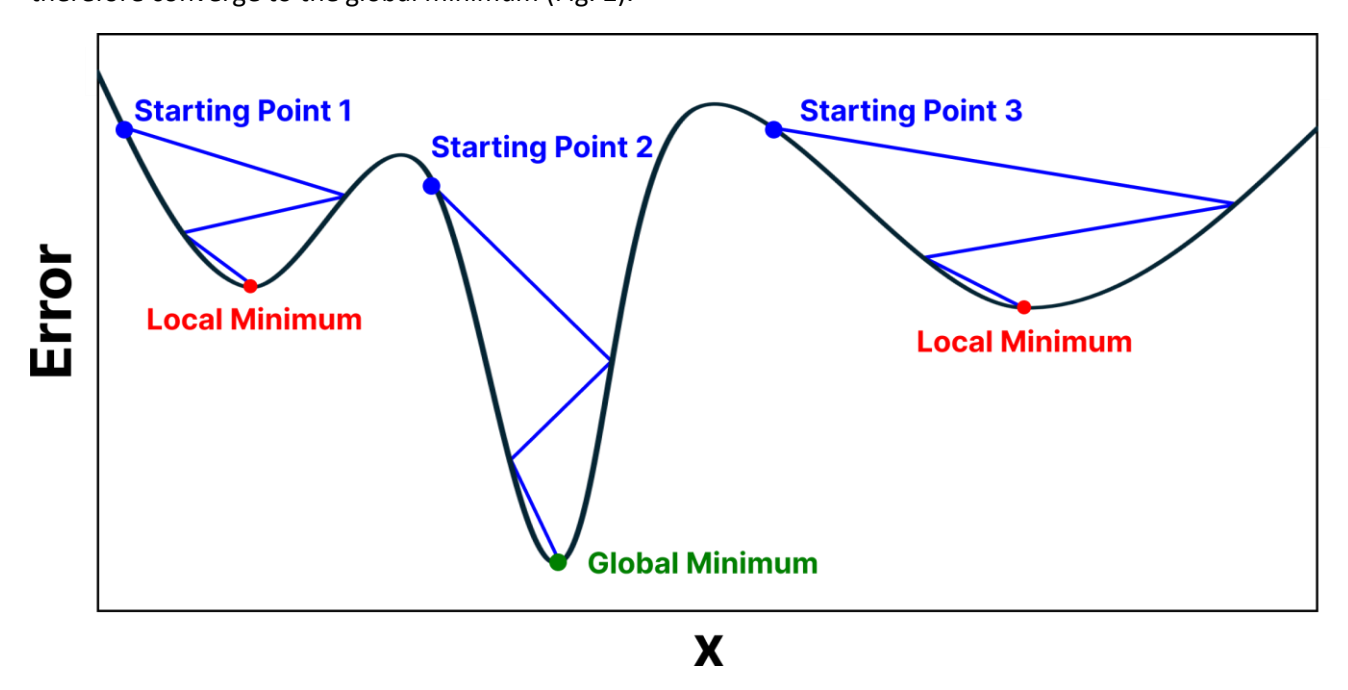


Figure 2: Convergence to the global minimum by choosing multiple starting points.

## **Adaptive Moment Estimation Algorithm**

Adam updates its step by using both the current gradient and its history. It maintains two running averages: one of the gradients (first moment) and one of squared gradients (second moment)<sup>10</sup>. These moments provide information about the descent's general direction and how large or noisy the gradients are. This

enables escape from local minima that trap simpler gradient descent methods. At each iteration k, the gradient of the objective function is first computed as:

$$\boldsymbol{g}_k = \nabla f(\boldsymbol{x}_k) \,. \tag{31}$$

The first moment is updated as:

$$\mathbf{m}_k = \beta_1 \mathbf{m}_{k-1} + (1 - \beta_1) \mathbf{g}_k$$
, (32)

which averages the gradients over time, where  $\beta_1$ , typically set to 0.9, controls how strongly past gradients influence the moving average. In parallel, the second moment is updated as:

$$v_k = \beta_2 v_{k-1} + (1 - \beta_2) g_k^2, \quad (33)$$

where  $\beta_2$ , typically set to 0.999, controls how strongly past squared gradients influence the moving average. The second moment reflects how large or unstable the gradients are across iterations. In Adam, the first and second moment estimates ( $m_k$  and  $v_k$ ) are initialized at zero, causing them to underestimate the true average gradients during the initial iterations. Without correction, this would result in smaller updates and slow down convergence. To compensate, Adam applies a correction that rescales the moments based on the number of iterations, ensuring appropriate step sizes from the start of the algorithm:

$$\widehat{\boldsymbol{m}}_k = \frac{\boldsymbol{m}_k}{1 - \beta_1^k} \qquad (34)$$

$$\widehat{\boldsymbol{v}}_k = \frac{\boldsymbol{v}_k}{1 - \beta_2^k} \,. \tag{35}$$

This ensures larger values of the first and second moments for early iterations. This correction will disappear after multiple iterations, as  $\beta_1$  and  $\beta_2$  go to zero at higher powers.

Finally, parameters are updated by scaling the averaged gradient by the square root of the averaged squared gradient:

$$x_{k+1} = x_k - \alpha \frac{\hat{\boldsymbol{m}}_k}{\sqrt{\hat{\boldsymbol{v}}_k} + \epsilon}, \quad (36)$$

where  $\alpha$  is the learning rate and  $\epsilon$  is a small constant that prevents division by zero, typically set to  $10^{-8}$ . With this algorithm, Adam scales each step based on gradient information, enabling optimization without line search, reducing memory requirements. Adam also operates over the entire real line; therefore, the sigmoid transformation from Equations 29 and 30 should be used to enforce bounds.

## III. RESULTS & DISCUSSION

## A. Preliminary Evaluation of Magnet Configurations

Before optimizing the magnetic array, an initial evaluation was performed to determine how the relative orientation and spacing of magnets affected the resulting magnetic field. This analysis served to narrow the design space and improve optimization efficiency.

First, two general magnet configurations were evaluated: a lateral configuration, with magnets positioned alongside the microrobot's direction of motion (Fig. 3A), and a longitudinal configuration, with magnets placed at the front and rear of the microrobot's direction of motion (Fig. 3B). The lateral magnet configuration achieved a magnetic field of 20-21 mT over an 80 mm range, beyond which the field strength dropped toward 10 mT, resulting in gradients up to 957 mT/m (Fig. 3C-E). The longitudinal configuration exhibited larger variations in magnetic field strength and gradient, ranging from 13 mT between the magnets to 399 mT near the magnet surfaces, with gradients up to 33 T/m (Fig. 3F-H). This indicated that the lateral configuration produced a significantly more uniform field, with deviations and gradients up to 30 times lower than the longitudinal setup. In addition, the use of high-strength magnets in the longitudinal configuration posed serious safety risks.

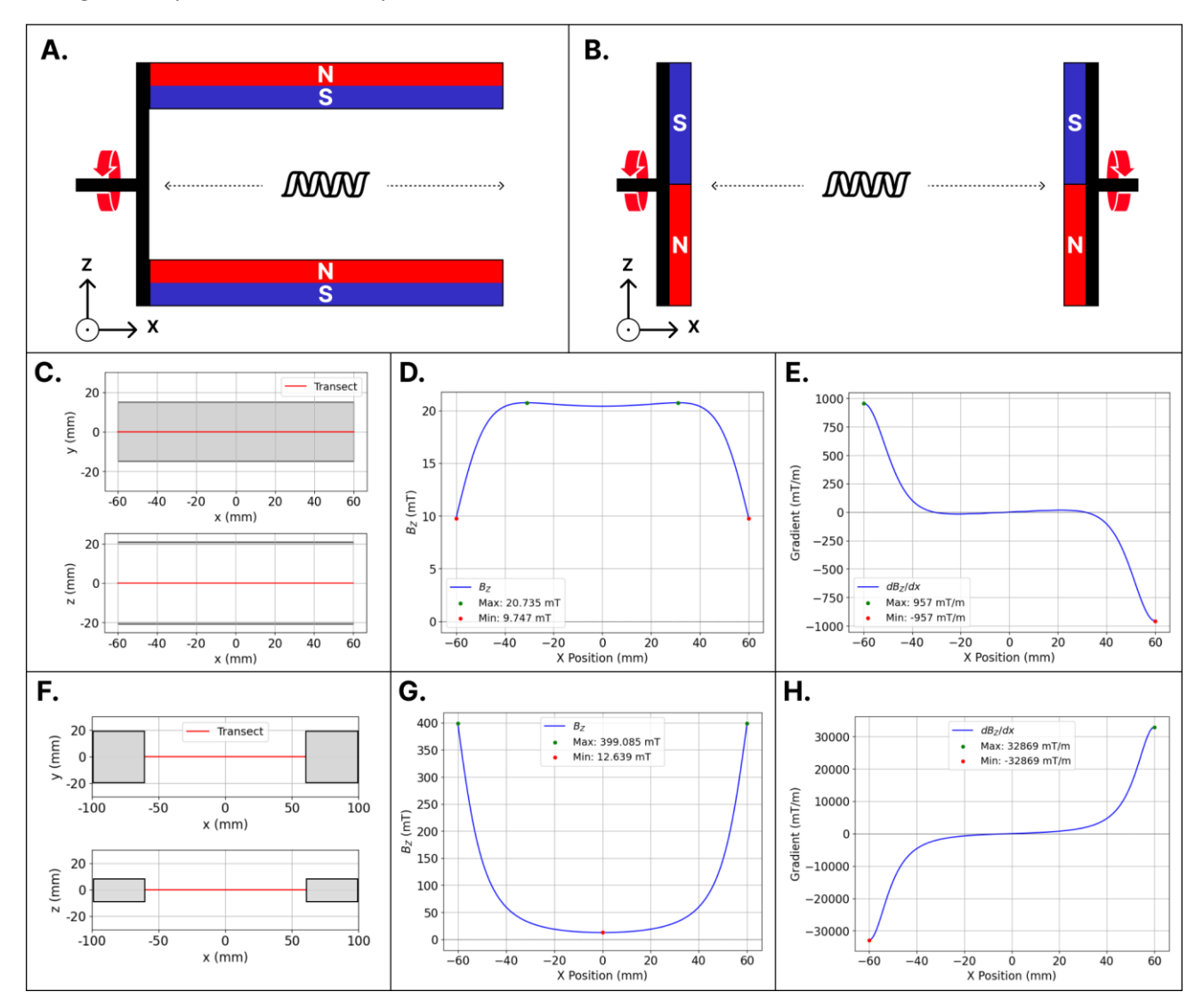


**Figure 3:** Magnetic field strength and gradient of lateral and longitudinal magnet configurations measured within ±60 mm, with the lateral configuration producing the most uniform field. **(A)** Conceptual overview of the lateral magnet configuration. **(B)** Conceptual overview of the longitudinal magnet configuration. **(C)** Schematic of the lateral setup with 30 × 175 × 1 mm N42 magnets placed 40 mm apart. **(D)** Magnetic field strength of the lateral setup along the x-axis. **(E)** Magnetic gradient of the lateral setup along the x-axis. **(F)** Schematic of the longitudinal setup with two 40 × 40 × 20 mm N42 magnets spaced 120 mm apart. **(G)** Magnetic field strength of the longitudinal setup along the x-axis. **(H)** Magnetic gradient of the longitudinal setup along the x-axis.

Increasing the length of the lateral magnet configuration to 175 mm produced a magnetic field between 19.8 and 20.5 mT over a 120 mm range, with the maximum field strength occurring near the edges of the transect, and a maximum gradient of 24 mT/m (Fig. 4A-C). This indicated that elongating the magnets led to an extended region where the magnetic field remained closer to the target value. However, this setup still exceeded the maximum allowable field strength deviation (see Chapter 1). A notable observation in this configuration was that the maximum field strength occurred off-center rather than along the central axis of the magnets. This outcome deviated from what would be expected if the magnets behaved as ideal dipoles, which would produce a central peak. The observed field shape can be attributed to the proximity of the magnets: at the midpoint between two thin magnets, the opposing flux from both sides of the magnets largely canceled out. Slightly off-center, the flux from the nearby poles remained nearly constant, while the opposing flux from the more distant pole decreased more rapidly. This resulted in off-center maxima. When the magnets were positioned further apart, the field resembled the expected dipole behavior, with the maximum magnetic field occurring at the center of the magnets (Fig. 4D-F).

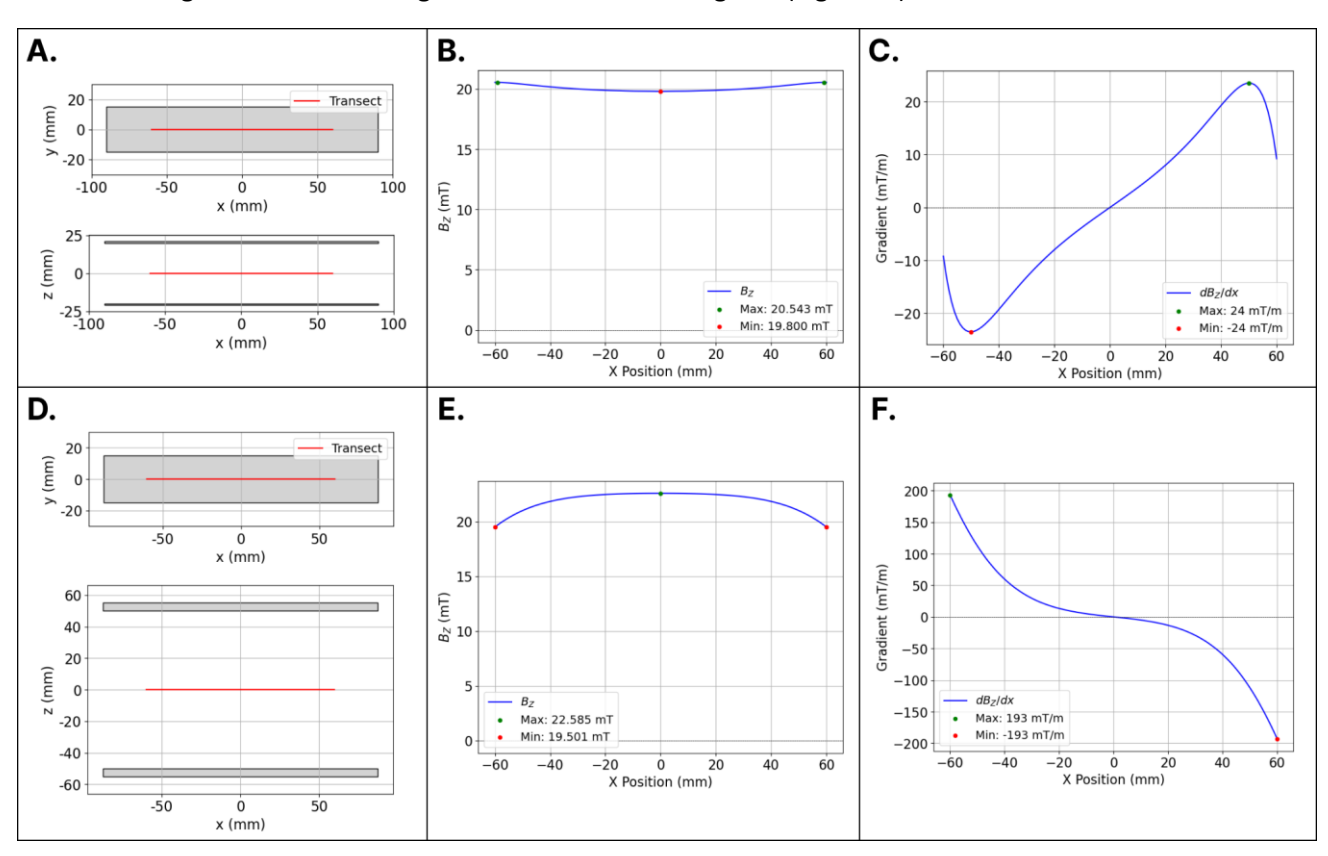


**Figure 4:** Magnetic field strength and gradient of an extended parallel magnet configuration measured within  $\pm 60$  mm, showing that elongating the magnets improved field uniformity. **(A)** Schematic of two  $175 \times 30 \times 1$  mm N42 magnets placed 40 mm apart. **(B)** Magnetic field strength along the x-axis. **(C)** Magnetic gradient along the x-axis. **(D)** Schematic of two  $175 \times 30 \times 1$  mm N42 magnets placed 100 mm apart. **(E)** Magnetic field strength along the x-axis. **(F)** Magnetic gradient along the x-axis.

An array-based magnet configuration consisting of cubical magnets that were all placed an equal distance from each other, produced a magnetic field ranging from 19.8 to 20.8 mT over a 120 mm range, with a maximum gradient of 35 mT/m (Fig. 5A-C), exceeding the allowable field strength deviation from Chapter 1. Reducing the spacing between the outermost magnets from 34 mm to 30 mm resulted in a magnetic field between 19.8 and 20.5 mT and a maximum gradient of 24 mT/m over the same range (Fig. 5D-F), closely matching the characteristics of the solid lateral magnet configuration (Fig. 4A-C). This indicated that moving individual groups of magnets improved the magnetic field characteristics.

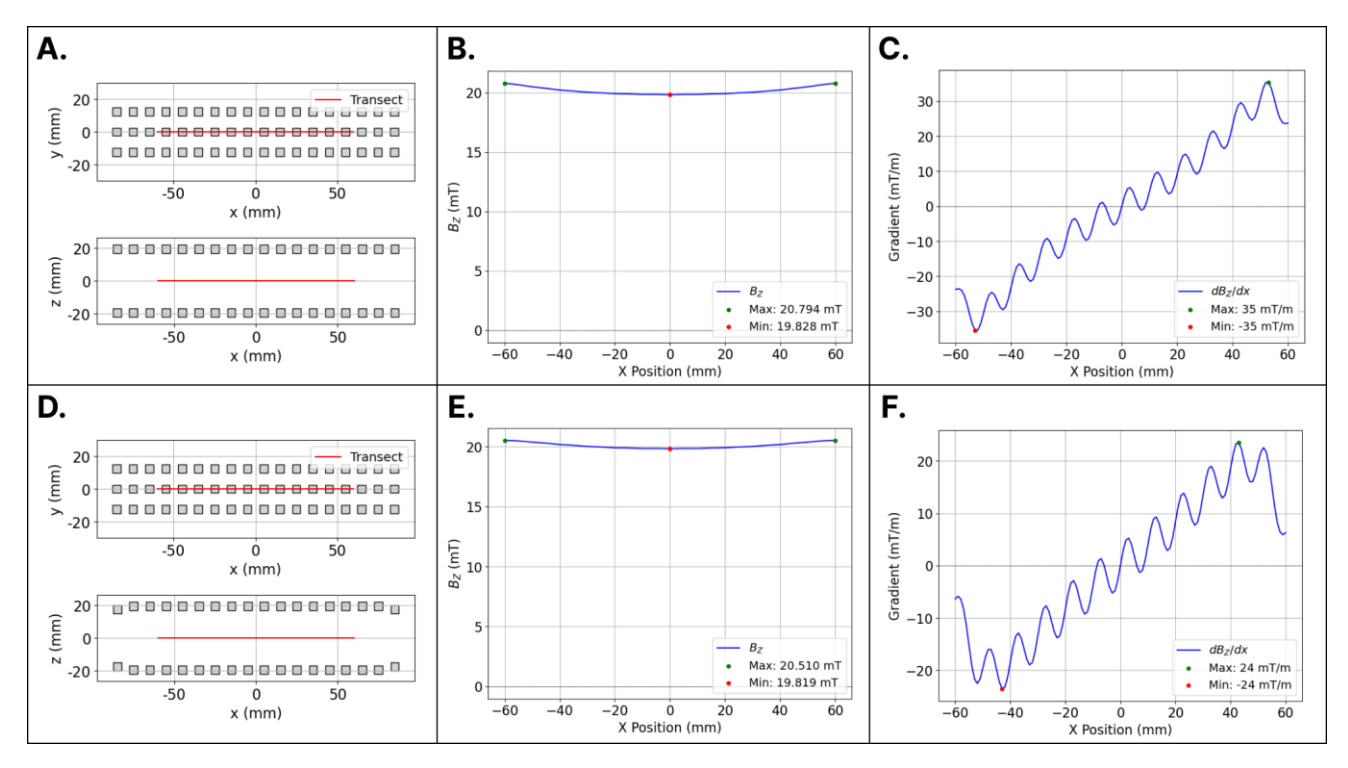


**Figure 5:** Magnetic field and gradient of two magnet array configurations measured within  $\pm 60$  mm, demonstrating that the individual placement of magnets can improve field uniformity. **(A)** Magnet array consisting of 18 columns and 3 rows of  $5 \times 5 \times 5$  mm N42 magnets placed 34 mm apart. **(B)** Magnetic field strength along the x-axis. **(C)** Magnetic gradient along the x-axis. **(D)** Magnet array with the outermost magnets placed 30 mm apart. **(E)** Magnetic field strength along the x-axis. **(F)** Magnetic gradient along the x-axis.

Too large spacing between adjacent magnets introduced oscillations in the magnetic field, resulting in poor field characteristics (Fig. 6A-P). To prevent these oscillations, the spacing between magnets along the x-direction was constrained to remain below one-tenth of the distance between the two arrays. With a minimum spacing of 30 mm (see Chapter 1), the maximum allowed x-direction spacing was 3 mm. Violating this constraint would result in oscillations in field strength and a sharp increase in gradients.

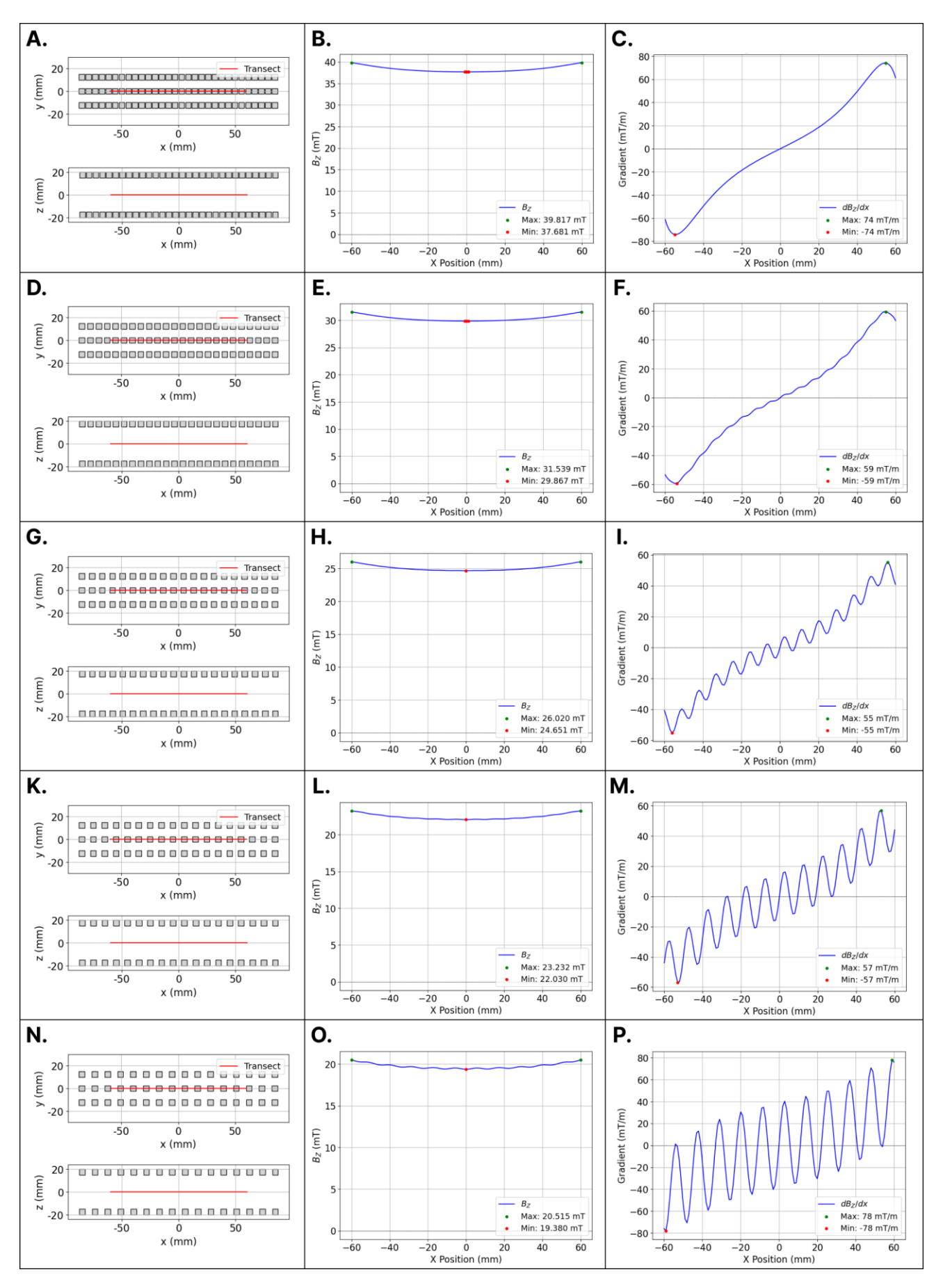


**Figure 6:** Magnetic field strength and magnetic gradient measured within ±60 mm for arrays of 5 × 5 × 5 mm N42 magnets placed 30 mm apart, using different magnet spacings. The figure reveals that exceeding a lateral magnet spacing of one-tenth of the distance between the two arrays results in large oscillations in the magnetic field, limiting precise microrobot actuation. **(A-C)** Array with 1 mm spacing. **(D-F)** Array with 2.5 mm spacing. **(G-I)** Array with 4 mm spacing. **(K-M)** Array with 5 mm spacing. **(N-P)** Array with 6.25 mm spacing.

### **B. Magnet Array Optimization**

Based on the previous chapter, a  $175 \times 30$  mm lateral magnet array configuration was optimized, consisting of 18 columns and 3 rows of  $5 \times 5 \times 5$  mm N42 magnets. Optimization aimed to minimize the objective function (Equation 18) by adjusting the spacing between opposing columns of the two magnet arrays, resulting in 9 independent parameters. The optimization included a constraint limiting the distance between opposing magnets to 30-44 mm. Five multivariate optimization algorithms were evaluated: grid search, hierarchical optimization, L-BFGS, multistart L-BFGS, and the Adam algorithm (Fig. 7). As a benchmark, the error from the configuration of Fig. 5A–C was used, which is referred to as the initial guess, as it represents the best achievable estimate within a reasonable time frame without optimization.

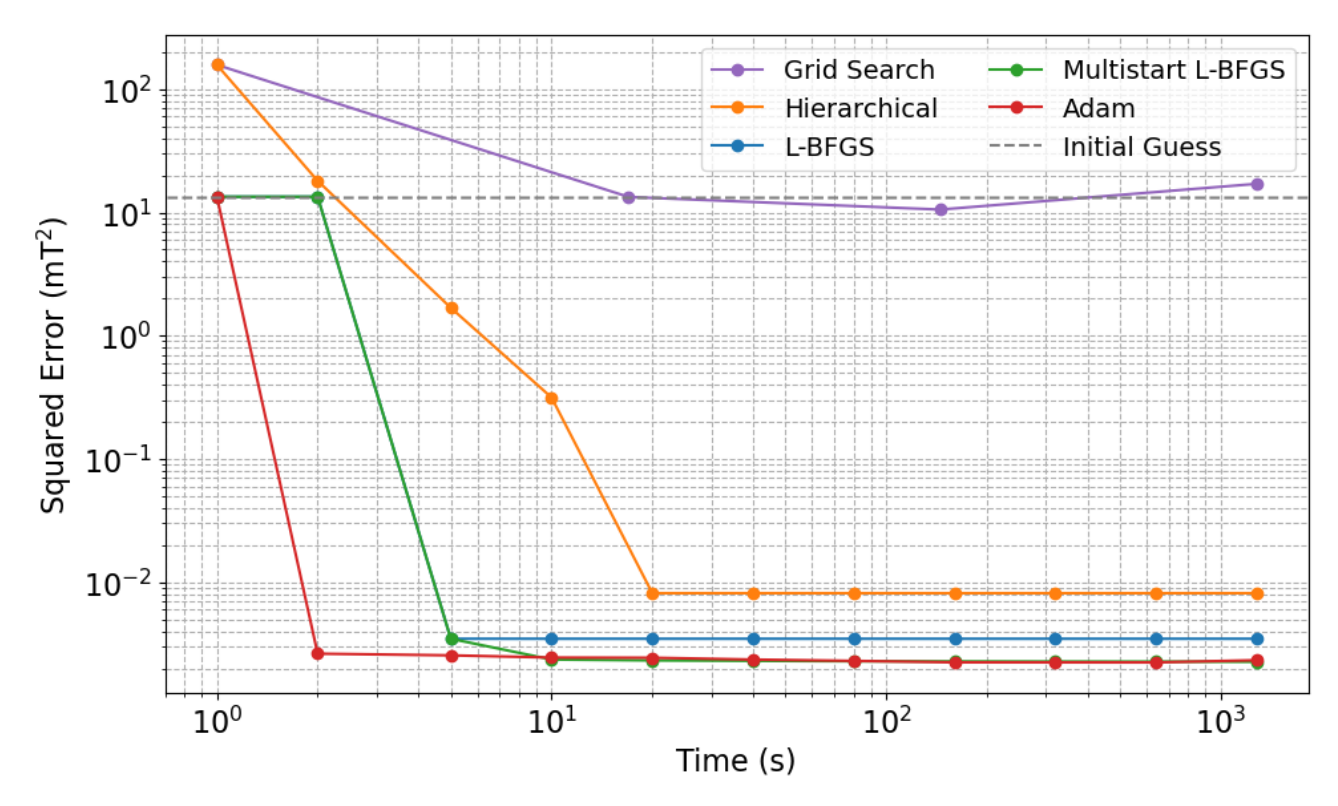


**Figure 7:** Final squared error and convergence time of five multivariate optimization algorithms applied to a symmetric magnet array consisting of 18 columns and 3 rows of  $5 \times 5 \times 5$  mm N42 magnets. Adam and multistart L-BFGS reached the smallest error, with Adam converging the fastest.

#### **Grid Search**

Grid search exhibited the poorest performance among all optimization algorithms, providing results scarcely better than the initial guess for the 20 mT target field. This was primarily due to the exhaustive nature of grid search, which, for five options per parameter, required approximately two million evaluations. Greater precision quickly exceeded practical computational limits, despite the fast evaluation time of  $7.25 \times 10^{-5}$  seconds per configuration enabled by the JAX library.

## **Hierarchical Optimization**

The hierarchical optimization method performed better than grid search but still yielded errors three to four times higher compared to the more advanced algorithms for the 20 mT target field. The higher error was attributed to the fact that the hierarchical optimizer became stuck in a local minimum instead of reaching the absolute minimum. Moreover, this method becomes infeasible for larger-scale problems, as scaling up to 18 independent parameters requires  $3.9 \times 10^8$  evaluations per step, hindering convergence.

## Limited-Memory Broyden-Fletcher-Goldfarb-Shanno Algorithm

The standard L-BFGS also got trapped in local minima. Therefore, the performance of the algorithm relied on the initial guess for the optimal configuration (Fig. 8). A starting value of 34 mm, an initial guess close to the absolute minimum, resulted in convergence within 5 seconds and a final squared error of  $3.5 \times 10^{-3}$  mT<sup>2</sup>. A starting value of 40 mm also converged in 5 seconds, with a higher final error of  $6.5 \times 10^{-3}$  mT<sup>2</sup>. An initial

guess of 42 mm led to a final error of 85 mT<sup>2</sup> and required 10 seconds to converge, exceeding the error observed with grid search (Fig. 7). This limitation emphasized the need for optimization strategies capable of more broadly exploring the design space.

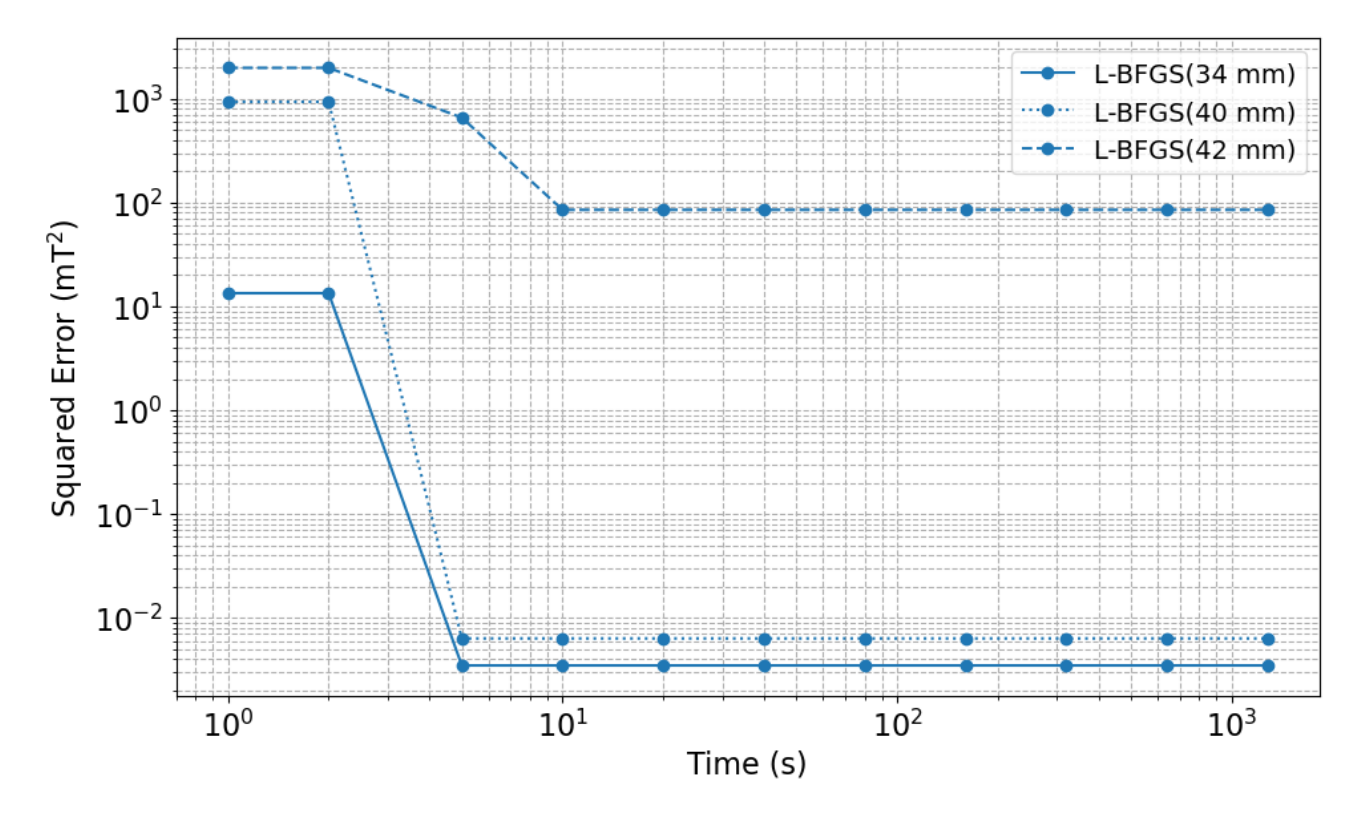


**Figure 8:** Final squared error and convergence time of the L-BFGS algorithm for different initial guesses of the magnet distance to the x-axis. The algorithm was applied to a symmetric magnet array consisting of 18 columns and 3 rows of  $5 \times 5 \times 5$  mm N42 magnets. The figure illustrates that a poor initial guess can result in inadequate performance.

This was solved with the multistart L-BFGS algorithm, which explores the design space more broadly by simultaneously evaluating multiple initial guesses. Multistart L-BFGS achieved lower errors with a fast convergence time ( $2.2 \times 10^{-3}$  mT<sup>2</sup> in 10 s). Its performance was determined by increasing the number of initial guesses. Therefore, proper determination of the maximum number of iterations per initial guess required careful consideration, as it directly affected the algorithm's speed. The smallest tested budget of 20 iterations per initial guess yielded the fastest convergence, converging within 10 seconds (Fig. 9).

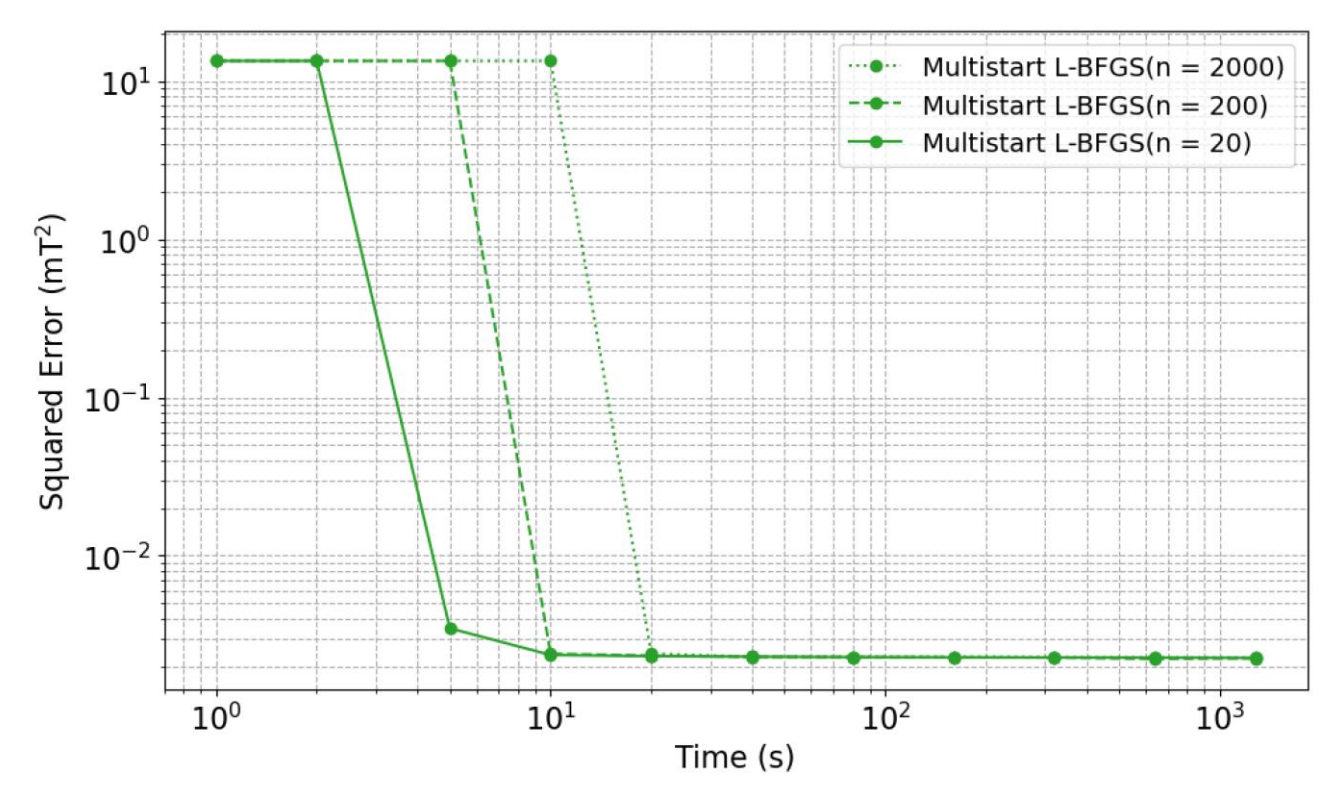


**Figure 9:** Convergence time of the multistart L-BFGS algorithm for different iteration budgets. The algorithm was applied to a symmetric magnet array consisting of 18 columns and 3 rows of  $5 \times 5 \times 5$  mm N42 magnets. The figure indicates that an iteration budget of 20 resulted in optimal performance.

## **Adaptive Moment Estimation Algorithm**

The Adam optimizer attained convergence to an error of  $2.2 \times 10^{-3}$  mT<sup>2</sup> within two seconds (Fig. 7), representing the fastest performance among the tested optimization algorithms for the 20 mT target field. The sensitivity of the Adam algorithm to the initial guess was also evaluated, and all configurations converged to the same final squared error of  $2.2 \times 10^{-3}$  mT<sup>2</sup>. This confirmed the ability of the algorithm to escape local minima. However, convergence time varied with the initial guess: the 34 mm condition resulted in convergence within 2 seconds, while the 40 mm and 42 mm initializations each required 20 seconds (Fig. 10).

The effect of the learning rate on the convergence behaviour of the Adam algorithm was also evaluated. Learning rates of 0.001 and 0.01 both converged to a final squared error of  $2.2 \times 10^{-3}$  mT<sup>2</sup>, with convergence times of 5 seconds and 2 seconds, respectively. In contrast, a learning rate of 0.1 did not converge within the experimental time frame and resulted in a final error between  $2.2 \times 10^{-3}$  and  $1.0 \times 10^{-2}$  mT<sup>2</sup> (Fig. 11). This indicated that the optimal learning rate for the optimization in this study was 0.01.

Overall, both Adam and multistart L-BFGS were shown to be effective optimization methods, capable of rapidly identifying near-optimal configurations. The high fidelity of these algorithms was further confirmed by observing Gibbs-like phenomena when targeting a step-shaped magnetic field (Appendix A), reinforcing the conclusion that the optimization methods approached fundamental theoretical limits. Finally, scaling the optimization to 90 independent variables with bounds between 30 and 100 mm (a tenfold increase) would slightly favor multistart L-BFGS (Appendix B). However, such scaling is not required for the target field in this study, but could be beneficial for other applications.

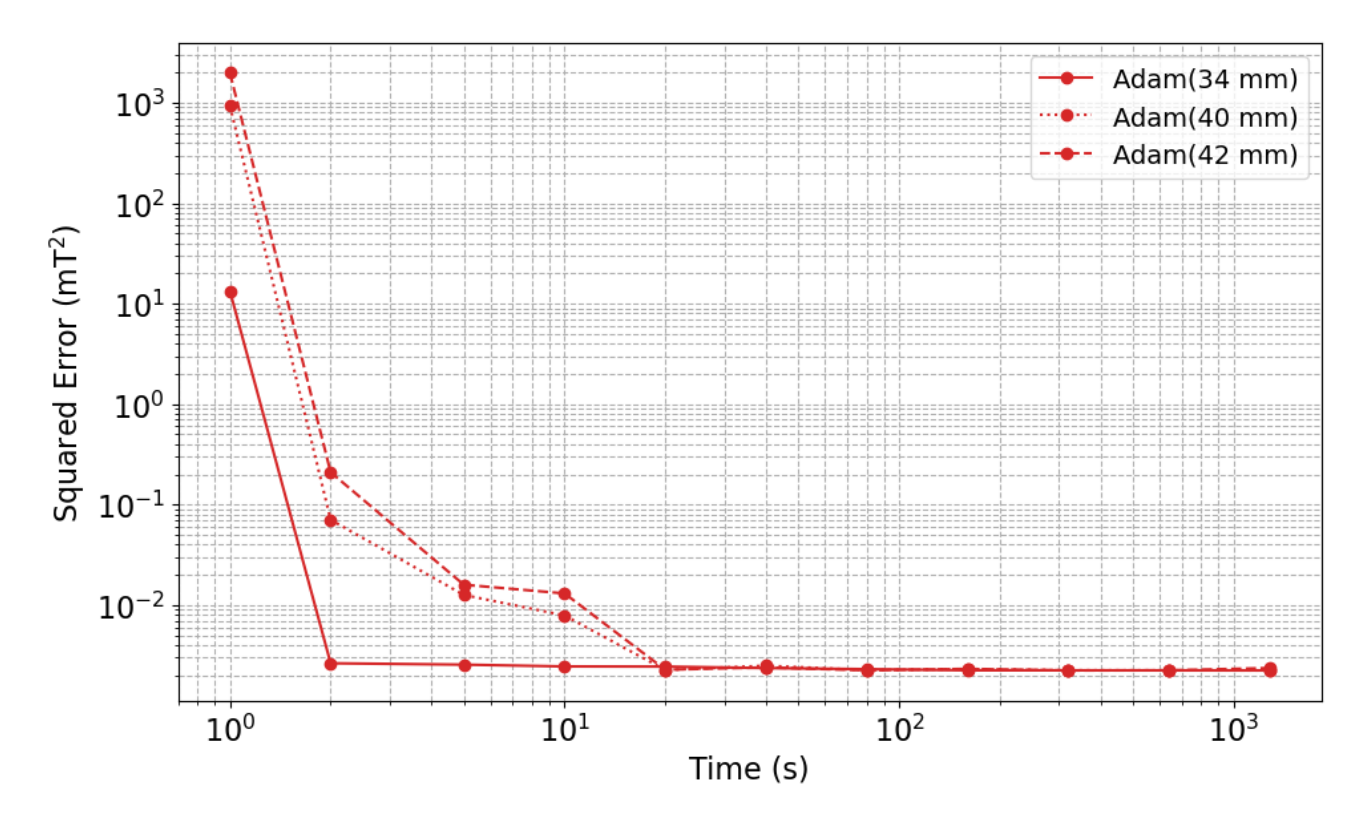


**Figure 10:** Convergence time of the Adam algorithm for different initial guesses. The algorithm was applied to a symmetric magnet array consisting of 18 columns and 3 rows of  $5 \times 5 \times 5$  mm N42 magnets. The figure illustrates that an inadequate initial guess can negatively impact performance; however, the final error remains unchanged.

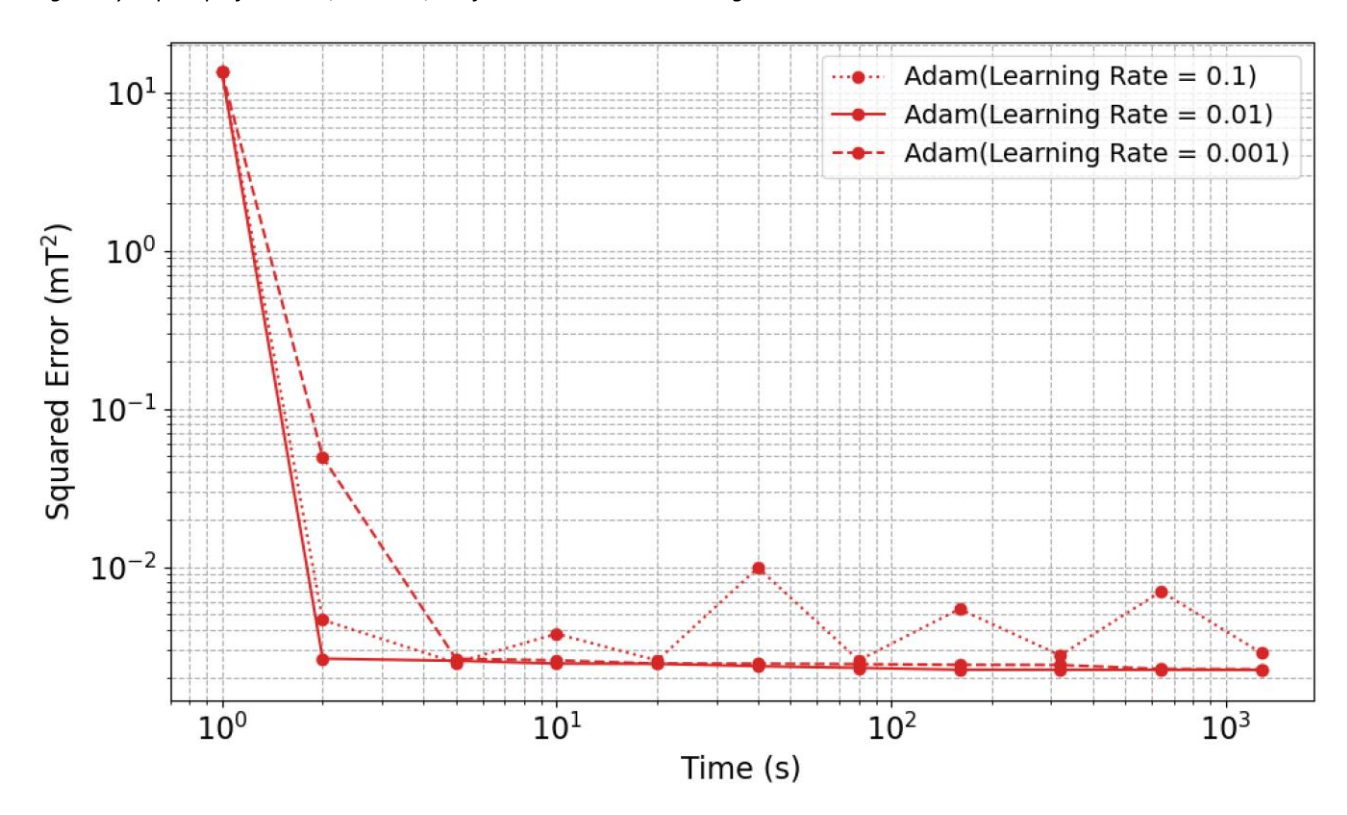


**Figure 11:** Convergence behavior of the Adam algorithm for different learning rates. The algorithm was applied to a symmetric magnet array consisting of 18 columns and 3 rows of  $5 \times 5 \times 5$  mm N42 magnets. The figure shows that a learning rate of 0.01 resulted in optimal performance.

## **C. Constructed Magnetic Array**

The constructed magnet array was optimized using the Adam algorithm due to its superior performance. This array was fabricated with a 3D printer and validated with a Gaussmeter (Fig. 12A-B). The measured magnetic field ranged from 19.9 to 20.2 mT, with a maximum deviation of 0.2 mT from the target field, which was well within the requirements (see Chapter 1). This confirmed that the Adam algorithm was capable of producing magnetic configurations that generated uniform magnetic fields with a specified field strength of 20 mT.

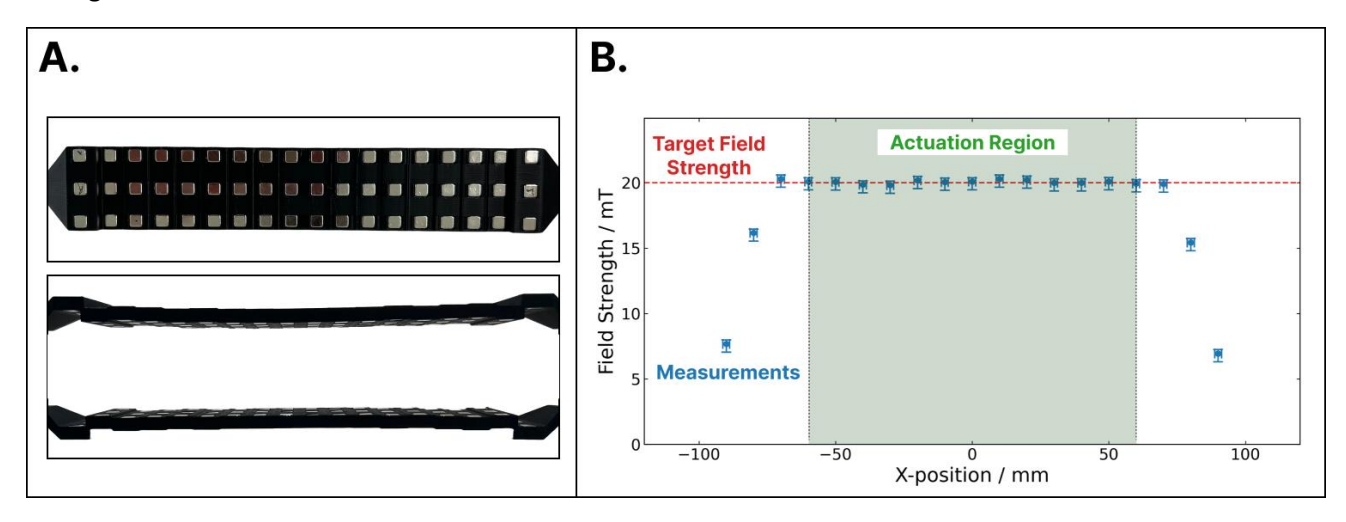


**Figure 12:** Magnetic field strength and gradient of the constructed Adam-optimized magnet configuration measured within  $\pm 60$  mm. **(A)** Picture of the constructed array consisting of 18 columns and 3 rows of  $5 \times 5 \times 5$  mm N42 magnets. **(B)** Measured magnetic field strength along the x-axis and its uncertainty. The figure shows that the constructed magnetic array was able to accurately produce the target field.

## IV. CONCLUSIONS

This Supplemental Material presents a design method for low-cost magnetic setups capable of generating uniform magnetic fields. Using multivariate optimization with the Adam algorithm and JAX acceleration, a lateral magnet array was optimized to generate a uniform 20 mT magnetic field with minimal gradient across a 120 mm region. Experimental measurements confirmed that both the field strength and its uncertainty remained fully within the specified target range, closely matching theoretical predictions and underlining the effectiveness of this design approach.

Some limitations must be acknowledged. First, the setup was limited to one-dimensional optimization in the x-direction, neglecting magnetic fields in the y- and z-directions. Second, the used magnets were not perfect cubes and had rounded edges; including this type of geometry in the algorithm could improve accuracy. Third, the optimization algorithm is currently limited to configurations with opposing magnets magnetized along the z-direction, restricting its broader applicability. Future work should investigate full 3D field shaping and incorporate more complex magnet geometries into the optimization algorithm by leveraging JAX's GPU/TPU acceleration.

## V. EXPERIMENTAL

## A. Computational Setup

All computations were performed with an HP ZBook Power G7 on CPU (Intel Core i7) with Python (3.12.3), JAX (0.4.35), and Optax (0.2.4).

## **B. Magnet Characteristics**

 $5 \times 5 \times 5$  mm magnets were obtained from supermagnete (Gottmadingen, Germany). The magnets had a 12 µm nickel layer; therefore, they were modelled as 4.98 x 4.98 mm in the optimization algorithm. The magnets were rated as N42; however, it was found that the magnets were not perfectly square but had rounded edges. The roundness of the edges was not included in the computational model. Instead, the remanent magnetization was modelled as 1.15 T. This value was obtained by fine-tuning the computational model parameters so that the simulated field matched the measurements produced by two magnets positioned directly between the measuring probe of a Lake Shore 455 DSP Gaussmeter (Figure 13).

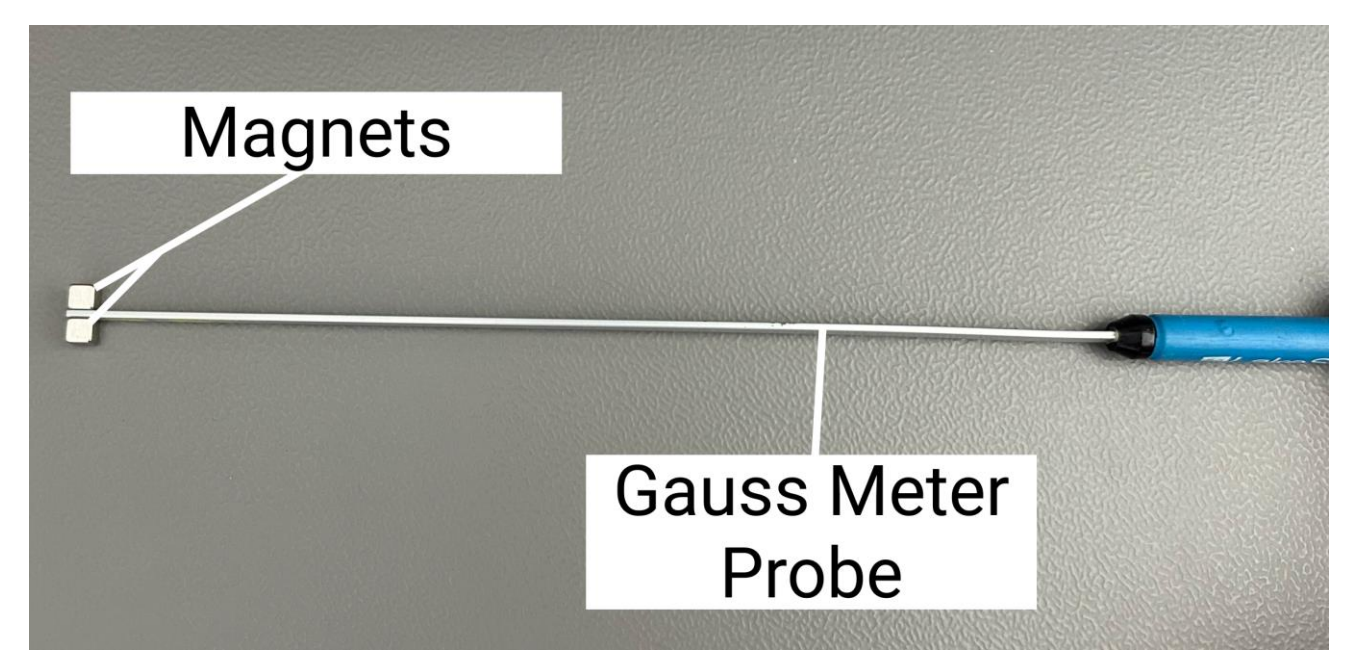


**Figure 13:** Calibration setup for determining the remanent magnetization using two  $5 \times 5 \times 5$  mm N42 magnets measured with a Gaussmeter.

## C. Array Fabrication

The magnetic arrays were fabricated using a Bambu Lab X1C 3D printer. To ensure precise spacing of the columns of magnets between the two arrays, which was optimized by the algorithm, this dimension was printed in the x-y plane (Fig. 14), which is more accurate than the z-direction. The difference in precision between print directions arises because accuracy in the x- and y-directions depends solely on the accuracy of the stepper motors, while precision in the z-direction is also influenced by variations in extrusion flow. Additionally,  $5 \times 5$  mm square holes were included to secure the magnets via press fit.

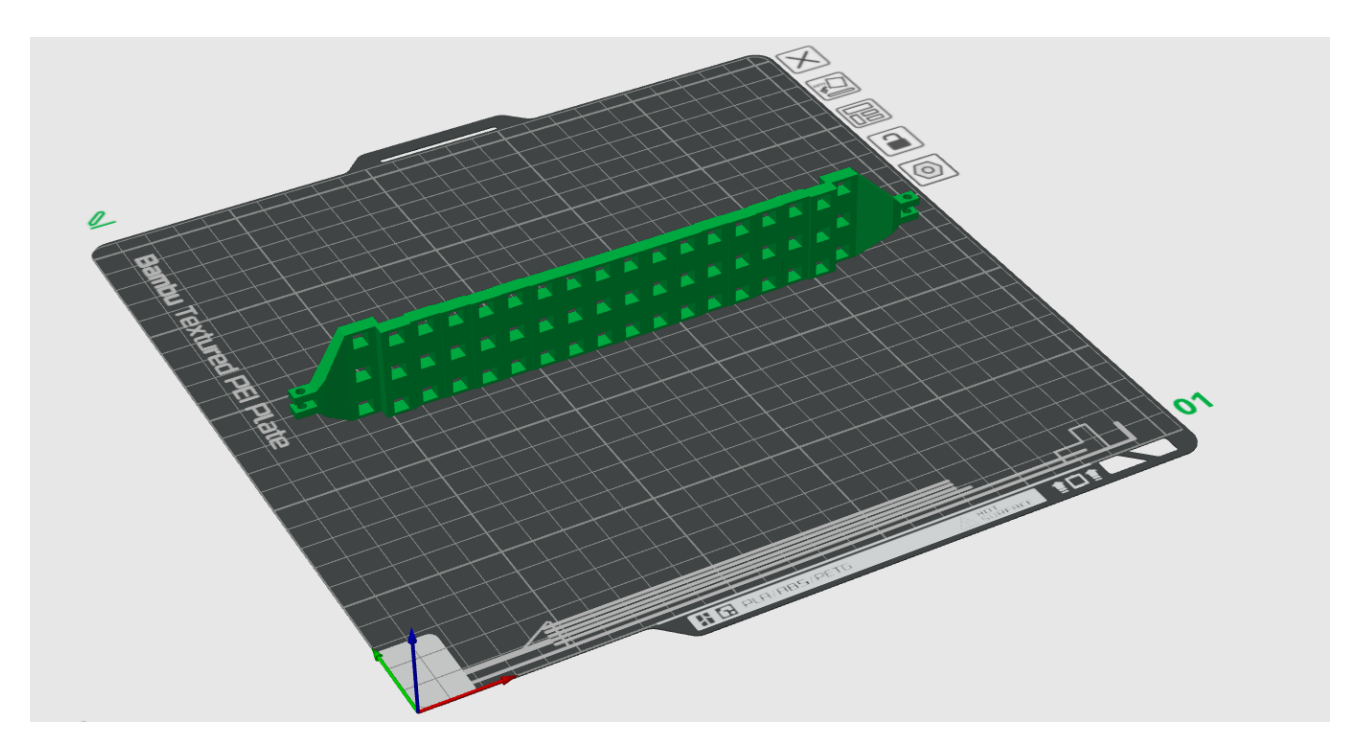


**Figure 14:** Print orientation of the magnetic array, with the magnetic columns aligned in the z-direction to maximize printing precision.

## D. Magnetic Field Validation

The magnetic field produced by the 3D-printed array was validated using a Lake Shore 455 DSP Gaussmeter. Measurements were taken every 10 mm, with the probe positioned between the magnetic arrays using a measuring guide (Fig. 15).

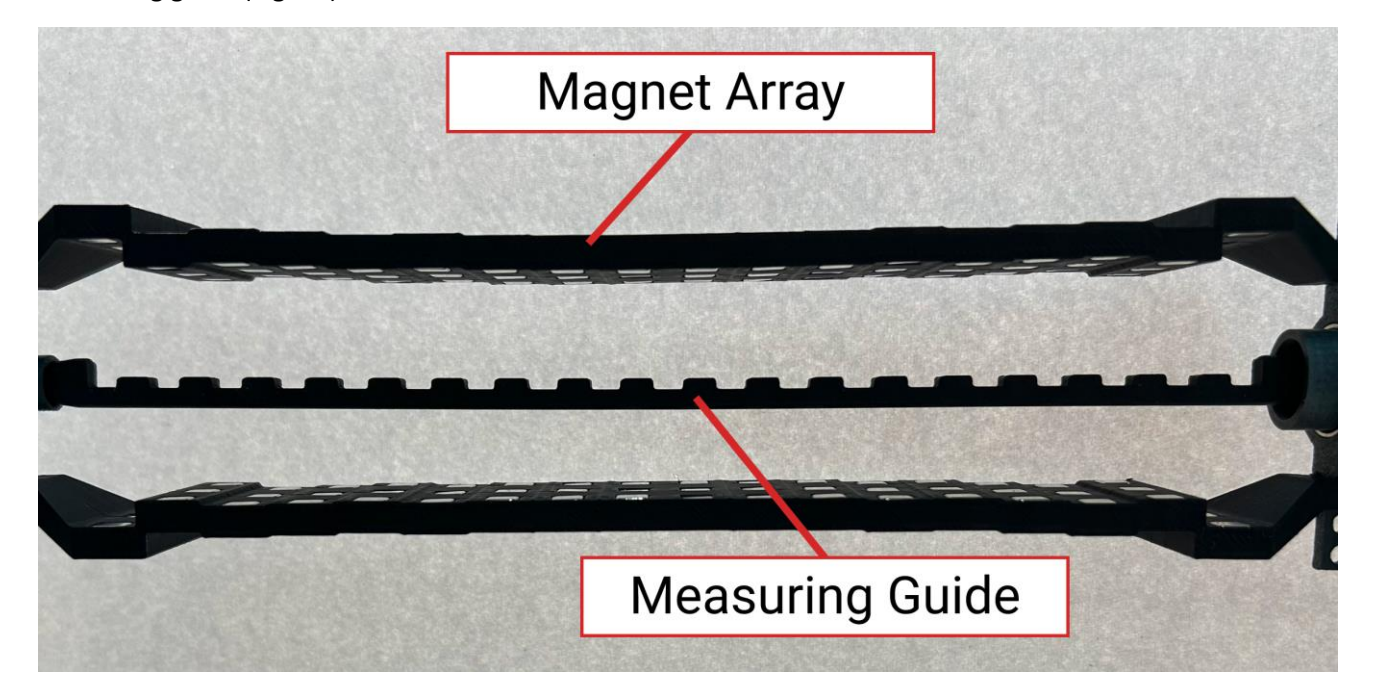


**Figure 15:** Magnetic field validation setup showing the magnetic array and the measuring guide with slots for the probe of the Gaussmeter.

## **REFERENCES**

- <sup>1</sup>Micro Magnetics, https://directvacuum.com/products/spincoil-xyz-200 (accessed 23 June 2025).
- <sup>2</sup>C. Zheng, Z. Li, T. Xu, L. Chen, F. Fang, D. Wang, P. Dai, Q. Wang, X. Wu, and X. Yan, Applied Materials Today 22, 10.1016/j.apmt.2021.100962 (2021).
- <sup>3</sup>JAX, https://docs.jax.dev/en/latest/index.html (accessed 23 June 2025).
- <sup>4</sup>E. P. Furlani, in *Permanent Magnet and Electromechanical Devices*, Electromagnetism, edited by E. P. Furlani (Academic Press, San Diego, 2001) pp. 97–205.
- <sup>5</sup>N. Kovvali, in *Theory and Applications of Gaussian Quadrature Methods*, Gaussian Quadrature, edited by N. Kovvali (Morgan & Claypool Publishers, San Rafael, 2011) pp. 21–35.
- <sup>6</sup>R. Bland, in *Solutions of Laplace's Equation*, Legendre Polynomials, edited by D. R. Bland (Springer Netherlands, Dordrecht, 1961) pp. 61–77.
- <sup>7</sup>Nocedal and S. J.Wright, in *Numerical Optimization*, Derivative-Free Optimization, edited by J. Nocedal and S. J.Wright (Springer, New York, NY, 2006) pp. 220–244.
- <sup>8</sup>Nocedal and S. J.Wright, in *Numerical Optimization*, Line Search Methods, edited by J. Nocedal and S. J.Wright (Springer, New York, NY, 2006) pp. 30–65.
- <sup>9</sup>D. C. Liu and J. Nocedal, *Mathematical Programming 45, 503 (1989)*.
- <sup>10</sup>D. P. Kingma and J. Ba, Adam: *A Method for Stochastic Optimization* (2017).

## **Appendix A: Step Function Optimization**

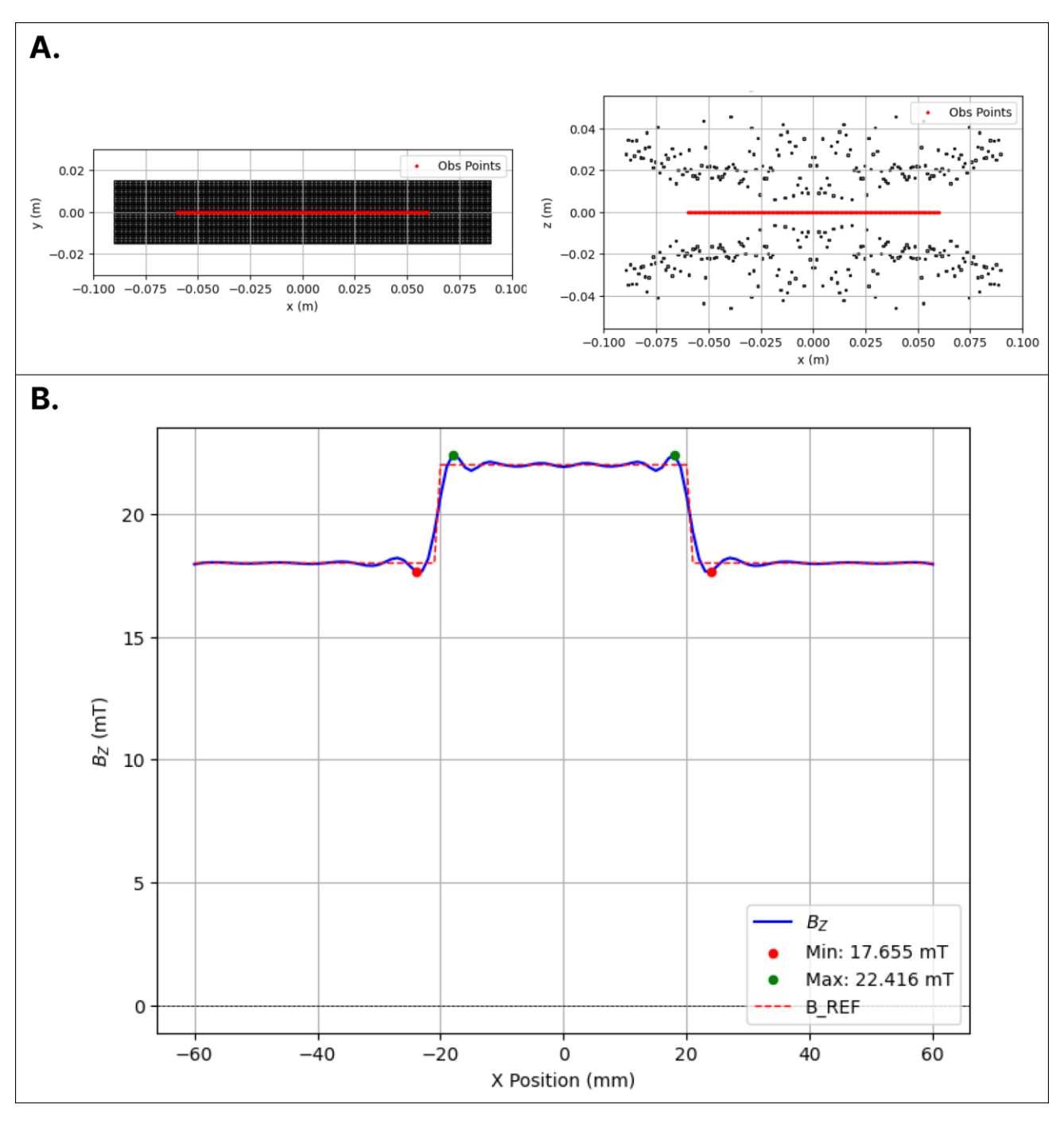


**Figure 16:** Gibbs-like ringing observed when optimizing for a 4 mT step-shaped magnetic field. The Gibbs phenomenon results in a characteristic combined overshoot of 18% of the step height. **(A)** Magnet array consisting of 180 columns and 30 rows of  $1 \times 1 \times 1$  mm N42 magnets. **(B)** Magnetic field strength along the x-axis measured within  $\pm 60$  mm.

## **Appendix B: Scaled Optimization Performance**

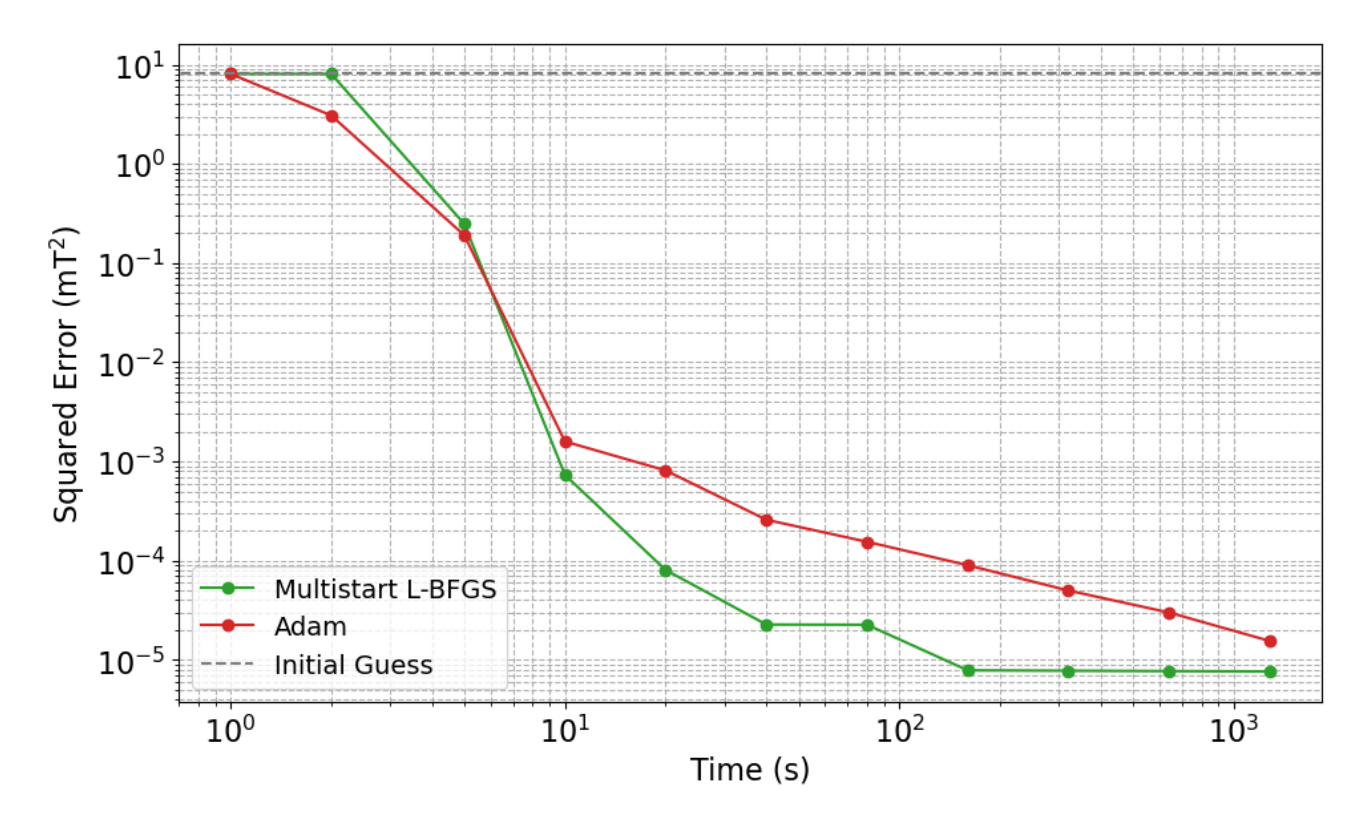
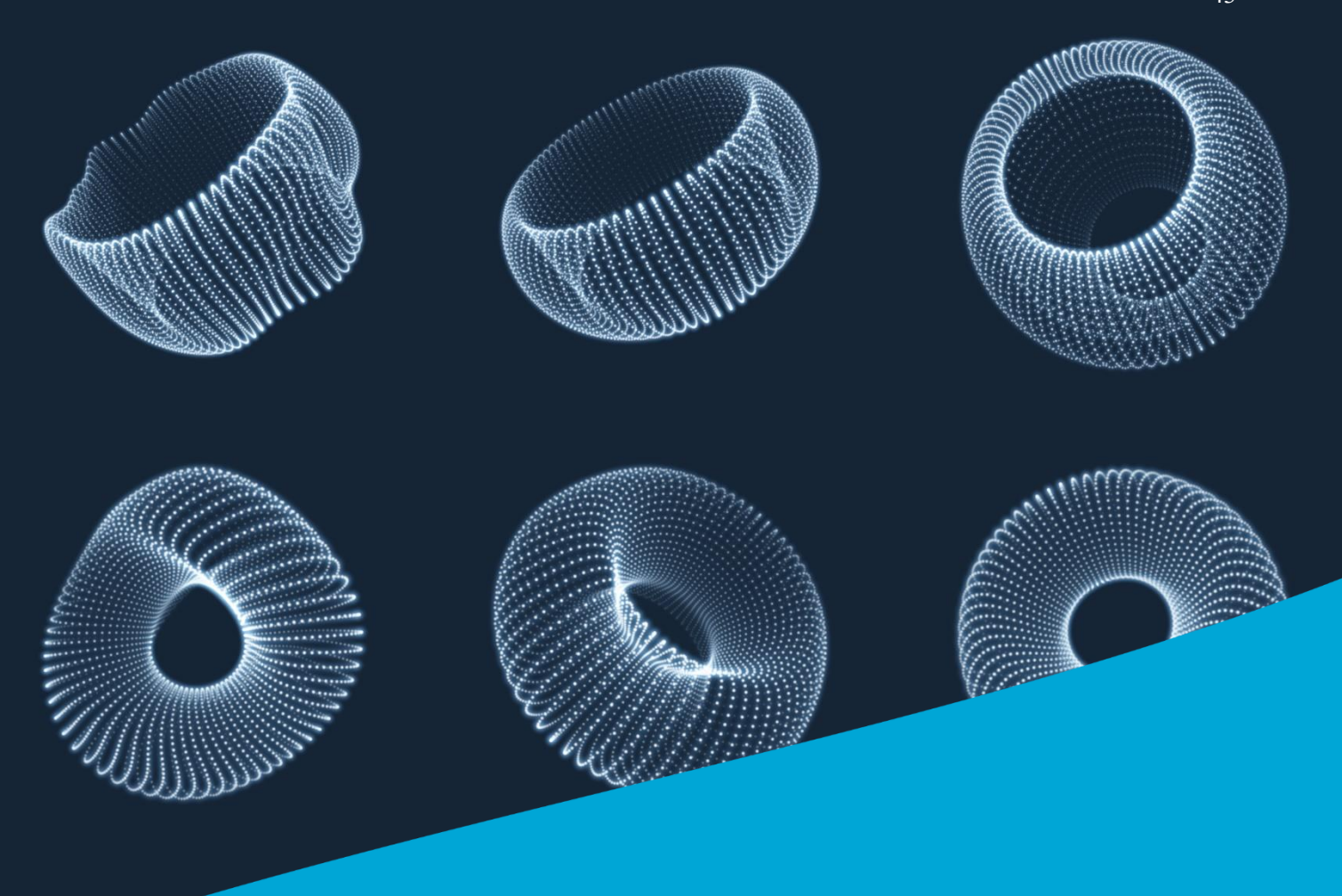


**Figure 17:** Convergence behaviour of multistart L-BFGS and Adam applied to a symmetric magnet array consisting of 180 columns and 30 rows of  $1 \times 1 \times 1$  mm N42 magnets. The columns were arranged symmetrically along the y-axis, resulting in 90 independent parameters. The distances to the x-axis were bounded between 30 mm and 100 mm. Multistart L-BFGS demonstrated faster convergence than Adam, which failed to converge within the evaluated time frame. However, both optimization algorithms achieved low errors within 10 seconds, underscoring the scalability of both algorithms.



# Propulsion Performance Comparison of Hardand Soft-Magnetic Microrobots Under Rotating Magnetic Fields

Supplementary Material 3: Microrobot Fabrication

Authors: Joost Wijnmaalen, Leon Abelmann, Iulian Apachitei

Dated: 11 July 2025



## **CONTENTS**

I.	Design	45
II.	Pre-Processing & Printing	47
III.	Post-Processing	48
Refe	erences	49

## I. DESIGN

Hard- and soft-magnetic microrobots, each with three distinct geometric configurations, were fabricated. These designs were based on the optimized geometries presented by Lin *et al.*<sup>1</sup>. The microrobot models were designed using SolidWorks (Dassault Systèmes, Vélizy-Villacoublay, France) and are accessible on GitHub.

The hard-magnetic microrobot designs consisted of a double helix, a tapered double helix, and a tapered ribbon-shaped geometry (Fig. 1). The double helix had a total length of 10 mm, a constant width of 6.5 mm, and a coil diameter of 0.8 mm. A longitudinal central cylinder with an outer diameter of 1.6 mm and an inner diameter of 1.2 mm was incorporated to secure a cylindrical NdFeB magnet (diameter 1 mm, length 3 mm). The internal hole was intentionally oversized to account for shrinkage caused by residual resin during the curing process. Additionally, three cylindrical support structures, each with a diameter of 0.6 mm, connected the central cylinder to the helical coils, enhancing structural rigidity during printing, post-processing, and actuation. The tapered double-helix maintained a total length of 10 mm and a maximum width of 6.5 mm, but featured a linear 30° taper toward the center from both ends. This design required only one central support structure (diameter 0.6 mm), as structural integrity was partly provided by the joining of helical coils at both ends. The tapered ribbon-shaped design was similarly 10 mm in length, had a wall thickness of 0.3 mm, a maximum width of 6.5 mm, and a curved 30° taper toward the center from both ends. This design did not require additional supporting structures.

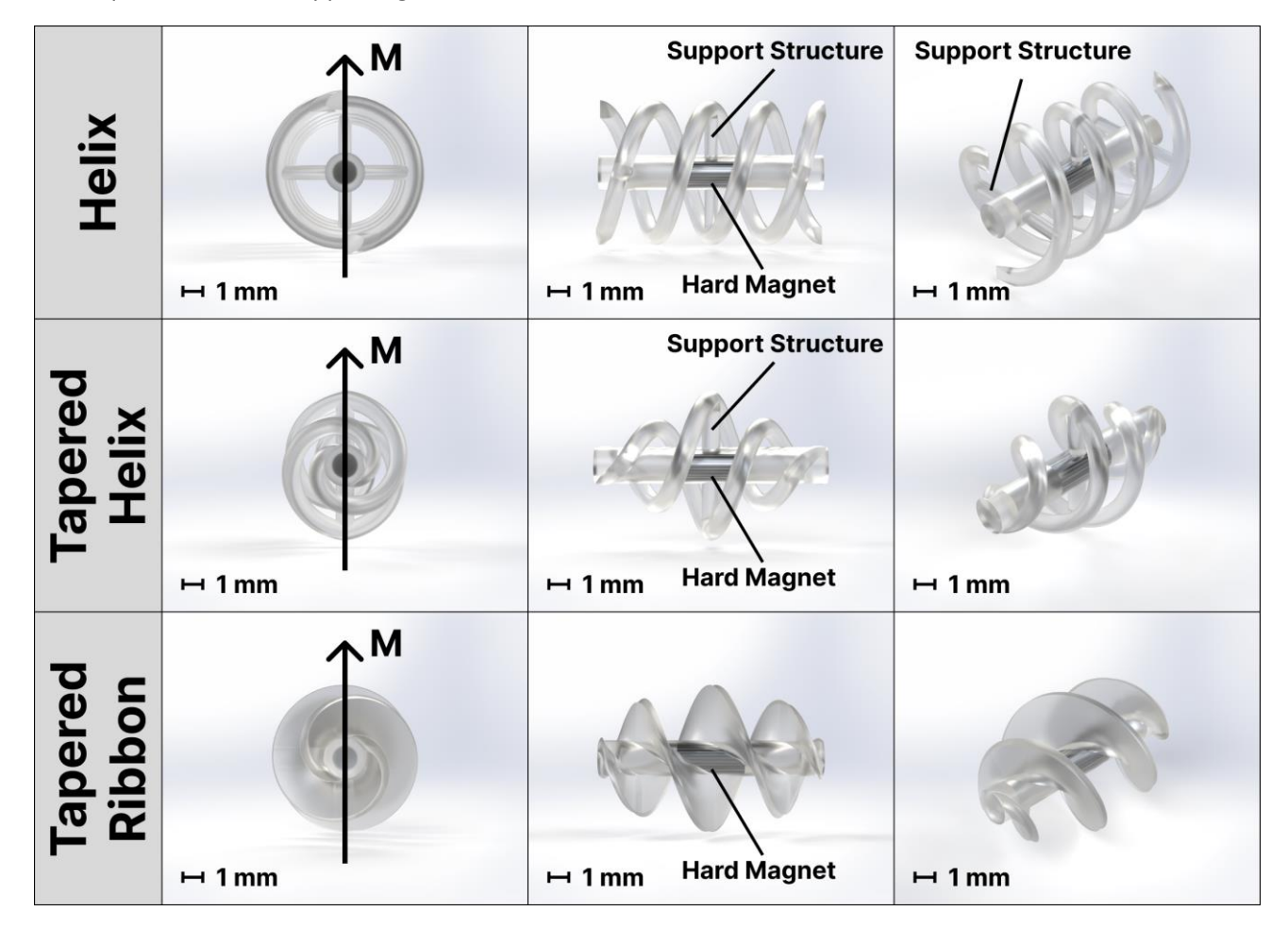


**Figure 1:** Overview of the three hard-magnetic microrobot designs: double helix, tapered double helix, and tapered ribbon-shaped geometry.

The soft-magnetic microrobots featured analogous geometric designs (Fig. 2). However, these designs included a transverse central cylinder with soft-magnetic material rather than the longitudinal cylinder used in the hard-magnetic designs. The central cylinder had an outer diameter of 1.6 mm and an inner diameter of 1.1 mm. The inner diameter was oversized to compensate for dimensional changes during curing. The soft-magnetic material had a diameter of 0.75 mm and a length of 5.33 mm, matching the volume of the hard magnet. Structural support structures included a single central axial support (0.6 mm diameter) and two transverse supporting structures (each with a 0.6 mm diameter) to maintain integrity during printing, post-processing, and actuation.

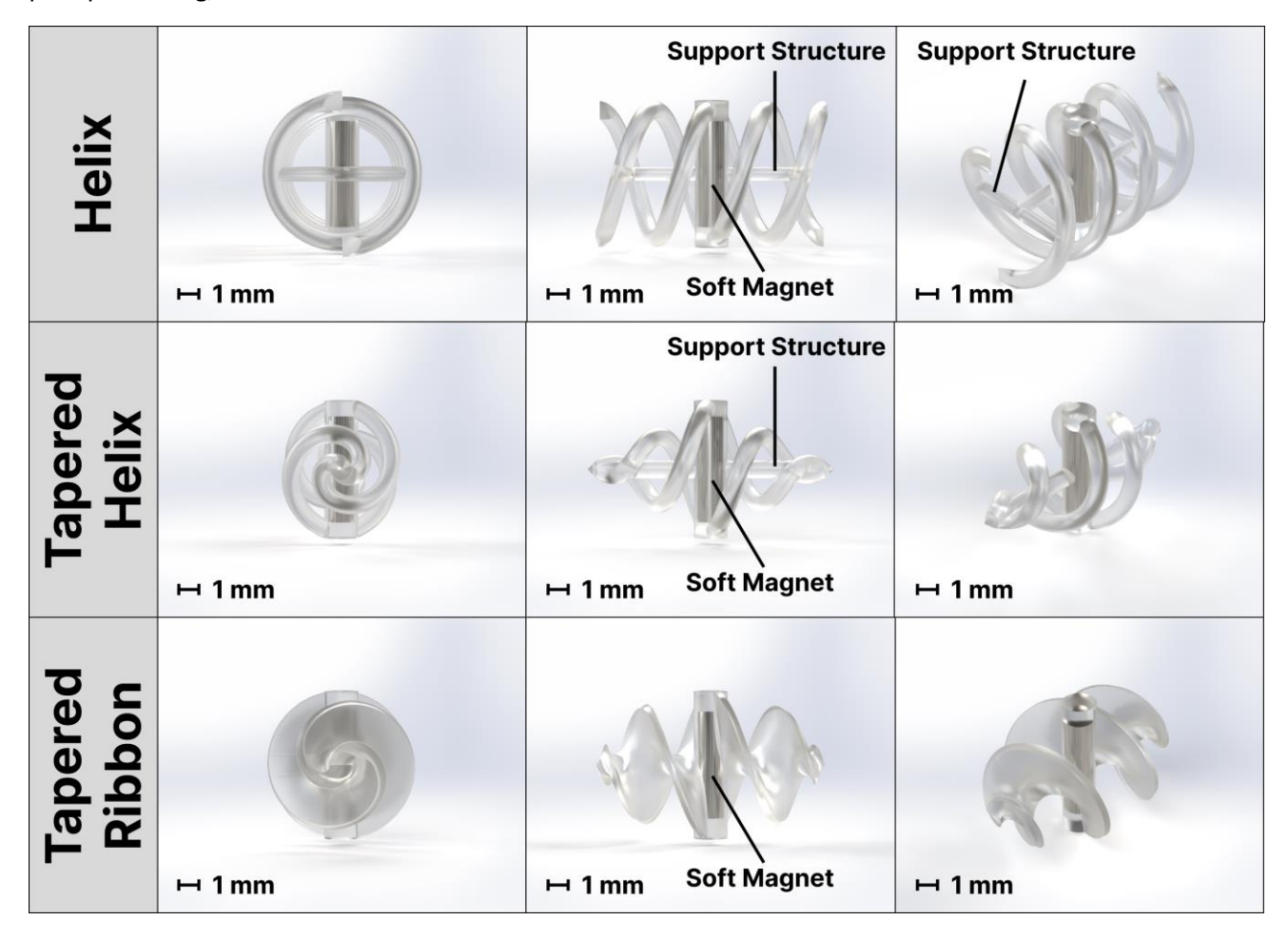


**Figure 2:** Overview of the three soft-magnetic microrobot designs: double helix, tapered double helix, and tapered ribbon-shaped geometry.

## II. PRE-PROCESSING & PRINTING

The finalized designs were exported as STL files, imported into PreForm software (Formlabs, Somerville, United States), and sliced. An auto-generated mini raft support structure was used (Fig. 3), with a touchpoint density of 1.00 and a touchpoint size of 0.40 mm. Printing was performed using a Formlabs Form 3 printer with adaptive layer thickness, utilizing clear V4 resin.

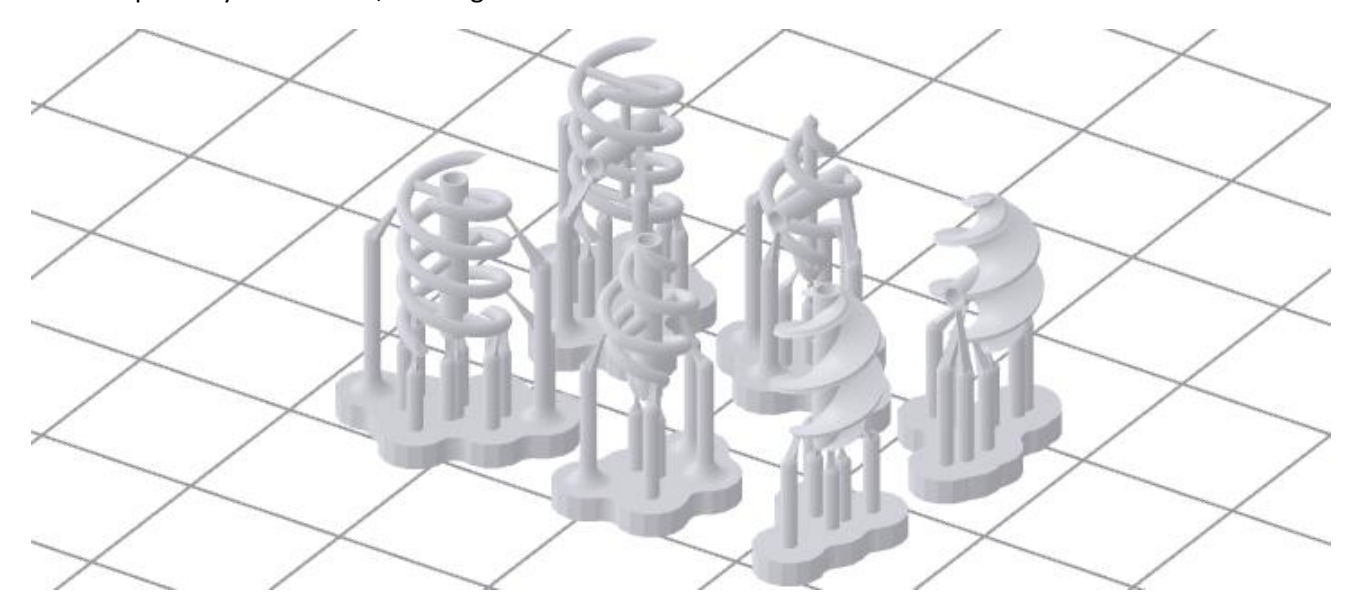


**Figure 3:** All hard- and soft-magnetic microrobot designs prepared in PreForm software, showing the generated supports and raft structures.

## III. POST-PROCESSING

After printing, the microrobots were washed in isopropanol for 10 minutes using the Form Wash (Formlabs, Somerville, United States). Following this, the supports were removed with a hobby knife, and any residual material inside the cylindrical hole was cleared with a needle to prevent obstruction after curing. Curing was done for 30 minutes in the Form Cure (Formlabs, Somerville, United States) for 30 minutes at 60°C. After curing, the three magnetic materials, NdFeB, ferrite, and pure Fe were inserted into the microrobots and secured with UHU Magnet Glue (UHU GmbH & Co. KG, Bühl, Germany) (Fig. 4).

	NdFeB Hard Magnet	Ferrite Soft Magnet	Pure Fe Soft Magnet
Helix	MAAA H 1 mm	→ 1 mm	H 1 mm
<b>Tapered</b> <b>Helix</b>	H 1 mm	H 1 mm	H 1 mm
<b>Tapered Ribbon</b>	H 1 mm	H 1 mm	H 1 mm

Figure 4: Resulting hard- and soft-magnetic microrobots after post-processing and magnet insertion.

## References

<sup>1</sup>J. Lin, Z. Zhu, X. Jing, M. Lu, and Y. Gu, Advanced Theory and Simulations **4**, 2100189 (2021).